Influence of wind direction on flow over a cliff and its interaction with a wind turbine wake

Arslan Salim Dar [*] and Fernando Porté-Agel [†]
Wind Engineering and Renewable Energy Laboratory (WIRE),
École Polytechnique Fédérale de Lausanne (EPFL), 1015-Lausanne, Switzerland

(Received 20 September 2023; accepted 29 May 2024; published 24 June 2024)

This work investigates the effect of wind direction on the flow over a cliff and its interaction with the wake of a wind turbine sited on the cliff. The cliff is modeled as a forward-facing step, and five wind directions are tested ($\theta = 0^\circ$, 15°, 30°, 45°, and -45°), where 0° represents a wind direction perpendicular to the cliff edge. The flow becomes increasingly three-dimensional with the increase in the wind direction magnitude and a cross-stream flow separation develops from the cliff leading edge. The turbulence kinetic energy decreases for wind directions higher than 15°, which is due to the absence of the streamwise flow separation for higher wind directions. The cross-stream flow development in the base flow affects the shape of the turbine wake. A two-dimensional Gaussian fit is performed on the wake velocity deficit, which shows a slight departure from self-similarity in the lateral direction. The wake recovery slows down for wind directions higher than 15°, which is consistent with the decrease in the wake growth rate for $\theta > 15^\circ$. The wake shows higher deflection and tilt angle for higher wind directions. Analysis of the streamwise momentum in the wake reveals that the advection terms play a role in slowing the wake recovery for higher wind directions.

DOI: 10.1103/PhysRevFluids.9.064604

I. INTRODUCTION

Concerns over the role of fossil-fuel-based energy sources in climate change have resulted in a push towards renewable energy sources. According to the International Renewable Energy Agency [1], new renewable energy installations are now economically more viable than their fossil fuel counterparts. Onshore wind energy, in particular, is one of the cheapest available sources of energy, with the levelized cost of energy falling 56% over the last decade [1] while accounting for 95% of the global wind energy capacity [2]. As countries across the world are setting ambitious goals towards renewable energy, wind energy is expected to grow at an unprecedented rate. To ensure successful growth of wind energy, an improved understanding of the interactions between wind turbines and the atmospheric boundary layer is needed. Wind turbines are often installed in groups forming wind farms, where due to spatial constraints, certain turbines have to operate in the wake of the upstream ones. The low velocity and enhanced turbulence experienced by the in-wake turbines result in reduced power production and enhanced fatigue loads. Turbine wakes are very complex and

[*]Contact author: arslan.dar@epfl.ch
[†]Contact author: fernando.porte-agel@epfl.ch

their characteristics depend on a multitude of factors such as the boundary-layer flow shear, surface roughness, terrain features, thermal stability, and turbulence intensity. Extensive efforts have been made to understand the interaction between wind turbines and the atmospheric flow under a variety of scenarios. For a detailed review of the state-of-the-art, the reader is referred to [3,4].

As onshore wind energy grows, the likelihood of wind farm installations in complex terrain also increases. This is motivated by the high available wind resources on top of hills or cliffs. For instance, cliffs are a common topographical feature near coastlines, and wind farms sited on them can benefit from high winds coming from the sea [5]. However, as stated by Porté-Agel *et al.* [4], most of the existing literature concerning wind turbine and wind farm flows is limited to flat terrain. Although the first studies investigating wind turbine wakes in complex terrain date back to the early 1990s [6–8], the topic has gained a renewed interest from the scientific community in recent years. For boundary-layer flows over complex topography, on the other hand, the literature is very rich, thanks to a wide range of analytical, numerical, and experimental efforts over the last 50 or so years.

The seminal work of Jackson and Hunt [9] laid the foundations for analytical studies of flow over hills with low slopes. They presented an expression for two-dimensional flow over arbitrary hills using perturbation methods. Their work was extended to three-dimensional hills by Mason and Sykes [10], and a more rigorous attempt was made by Sykes [11], who presented an asymptotic approach to flows over two-dimensional hills. Several studies attempted to validate the analytical model by Jackson and Hunt [9] against wind tunnel [12] and field [13] measurements. Attempts to include nonlinear effects into the analytical expressions were made by Xu *et al.* [14]. Among the most notable experimental campaigns are the Askervein hill project [15] and the Bolund hill experiment [16], which have served as benchmarks for numerical models attempting to capture flow in complex terrain. Since the 1990s, large-eddy simulation-based numerical approaches have become increasingly popular for investigating flow over topography [17–22]. It is to be noted that the list of studies concerning boundary-layer flows in complex terrain presented here is not exhaustive by any means, and for a more detailed review, the reader is referred to [23].

Changes in terrain elevation can lead to high levels of flow shear, high spatial variability in flow characteristics, formation of localized flow structures (such as regions of flow separation from cliffs and wakes of hills), and terrain-induced local changes in pressure gradient. Wake characteristics of wind turbines sited in complex terrain are strongly dependent on terrain characteristics, which is why a number of studies exploring turbine wakes in various idealized and real complex terrains have recently emerged. Mattuella *et al.* [24] tested a scaled-down model of a complex site located in Spain inside a wind tunnel. They concluded that very careful layout optimization for wind farms in complex terrains is required due to high variation in mean velocity and turbulence across the terrain. Tian *et al.* [25] experimentally investigated the power performance and wake of a wind farm sited on a sinusoidal hill. They showed that, compared to a wind farm in flat terrain, the hill influenced power and wake characteristics of the wind farm. Yang *et al.* [26] performed a numerical investigation of a wind turbine sited downstream from a three-dimensional hill. They showed that wake characteristics of the turbine were affected by both the height of the upstream hill and the spacing between the hill and the turbine. In their experimental study of wind turbines on periodic hills, Hyvärinen and Segalini [27] showed that a hilly terrain leads to a faster wake recovery. Shamsoddin and Porté-Agel [28] presented a combined analytical and numerical study of the wake of a wind turbine sited upstream of a hill. By dividing the flow over the hill into two regions corresponding to favorable and adverse pressure gradients, they showed that the wake recovery can be faster or slower compared to a flat terrain depending on the turbine location across the hill.

The wake trajectory of a wind turbine sited in Perdigão was investigated by Menke *et al.* [29], who showed that the wake follows the terrain under stable conditions, deflects upwards under unstable conditions, and shows no deflection in neutral conditions. Self-similarity of the wake velocity deficit is a common assumption in many analytical models. This assumption was verified by Dar *et al.* [30] via large-eddy simulation for a wind turbine wake in Perdigão. Liu and Stevens [31] investigated the effect of two-dimensional hills on the power performance of wind turbines and

wind farms sited across them. They found that, for turbines taller than the hill, a power boost can be observed due to speedup from the hill. For turbines smaller than the hill, on the other hand, their performance depends on the location along the hill. For a hill located in the middle of a wind farm, turbines located downstream from the hill experience the wake of the hill, which can affect their performance. Liu *et al.* [32] performed large-eddy simulation of wind turbine wake across two- and three-dimensional hills, and varied the ratio of turbine height to hill height. Interested in the wind turbine wake superposition over complex terrain, they investigated two different strategies, where one was based on superposition along the turbine hub height and the other along the streamline of the flow originating from the turbine hub height. From their results, they concluded that the second superposition method produced better results. More recently, Dar *et al.* [33] performed an experimental and analytical investigation of a wind turbine exposed to a range of pressure gradients. They showed that the wake deficit, expansion, and power coefficient vary systematically with the change in the pressure gradient. Atmospheric stability is another important factor that can have a significant effect on turbine performance and wakes, and its importance in complex terrain has instigated several recent studies [34–37].

Cliffs are a common topographical feature and a potential site of wind farms. Rowcroft *et al.* [38] presented a brief list of wind farms across the world that are sited close to cliff edges and potentially affected by the leading edge flow separation. Bowen and Lindley [39] were the first to investigate the effect of the cliff shape on the flow over it. Lange *et al.* [40] showed that the flow over the cliff is highly sensitive to minor modifications to the leading edge shape, which can have significant effects on the power available to the wind turbines. Schulz *et al.* [41] compared the performance of a turbine sited on flat terrain and on a steep escarpment. They found that the turbine sited on the escarpment experienced higher loads compared to the one on the flat terrain. Qian and Ishihara [42] performed detached-eddy simulation of a wind turbine sited close to the edge of an escarpment. They showed that the turbine wake characteristics depend on the ratio between turbine hub height and escarpment height. Dar and Porté-Agel [43,44] performed wind tunnel experiments to investigate the wake of a wind turbine sited close to an escarpment edge. They tested different leading edge shapes of the escarpment and showed that the wake characteristics of the turbine were affected by the escarpment shape. In addition, they used the experimental data to validate an analytical model for wind turbines experiencing a pressure gradient imposed by the base (without turbine) flow [45].

Flow over cliffs has often been approximated by the flow over forward-facing steps (FFS). A comprehensive body of literature has explored flow over forward-facing steps and its dependence on a number of flow and geometrical parameters [46–51]. Most of the literature deals with the flow direction perpendicular to the leading edge of the forward-facing step. In the atmospheric boundary layer, however, wind direction is not always perpendicular to the leading edge. Only a handful of studies deal with the effect of direction on flow over forward-facing steps. Rowcroft *et al.* [52] investigated the flow over forward-facing steps under different yaw angles and found that half a cliff height above and downstream from the leading edge is the optimal position with respect to flow speedup and turbulence intensity for turbine placement. Barthelmie and Pryor [53] performed a combined field and modeling study to understand the effect of changing wind direction on flow speedup over a cliff. The height of the cliff was 12 m, which is relatively small compared to the hub height of modern wind turbines. They observed that the flow speedup over the cliff was maintained for wind directions within $\pm 25^\circ$ from the direction perpendicular to the cliff edge. Hesp and Smyth [54] performed a numerical simulation of flow over scarps modeled as forward-facing steps. Concerning the wind direction, they found that the flow deceleration decreases with increasing obliqueness of the wind direction, and showed the flow pattern using streamlines. Previous studies have shown that a change in wind direction can impact the flow characteristics over a cliff. As wind turbines sited on cliffs have been reported to underperform in terms of power production [40], it is important to understand how the flow over a cliff changes under different wind directions and what impact it has on the performance and wake of a turbine. This study looks to uncover the underlying physical mechanisms behind the change in the mean flow and turbulence characteristics under oblique wind directions. In addition, we investigate how the complex three-dimensional flow

induced by a yawed cliff edge interacts with the wake of a wind turbine sited on it and affects its primary characteristics such as recovery, shape, and deflection.

This work aims at providing useful insights into the physics of the flow over a cliff modeled as a forward-facing step under different wind directions. A comprehensive analysis of the interaction between such flow and a wind turbine wake is also performed. Wind farms sited on cliffs are known to underperform in terms of power and experience high loads due to the lack of sufficient understanding of the base flow [40], which makes it extremely important to explore this topic in further detail. Wind tunnel experiments are performed, where the effect of wind direction is simulated by yawing the leading edge of the cliff. The rest of the article is organized as follows: the description of the experimental setup is provided in Sec. II; the results from the study are presented in Sec. III; and finally, a summary and some concluding remarks are given in Sec. IV.

II. EXPERIMENTAL SETUP

The experiments are performed in the closed-loop boundary-layer wind tunnel at the WiRE laboratory of EPFL. The wind tunnel has a maximum wind speed of 25 ms^{-1}, with an area contraction ratio of 5:1 at the inlet of the test section. The height and width of the test section are adjusted to yield an approximately zero pressure gradient along the length of the test section. At about 20 m downstream from the test section, the height and width are 2 and 2.56 m, respectively. The test section is 28 m in length, with a smooth aluminum floor. A turbulent boundary layer develops along the length of the test section without the use of any external tripping mechanism. The flow in the wind tunnel is driven by a 130-kW fan.

A three-bladed miniature horizontal axis wind turbine named WiRE-01 is used in the experiments [55]. The turbine has a rotor diameter D of 15 cm and a hub height z_h of 12.5 cm. The blade profile is a thick plate with a circular arc shape with a 5% camber and 5% thickness with respect to the chord length. The chord length varies from 12 mm at the root to 8.4 mm at the tip. The rotor is manufactured by three-dimensional printing using a liquid photopolymer resin. The nacelle of the turbine is a direct current motor manufactured by Maxon motors (model DCX10L), which has a diameter and length of 10 and 25 mm, respectively. The motor is controlled by a servo controller also manufactured by Maxon motors (model ESCON 36/2 DC) via a digital encoder (model ENX10).

The cliff is modeled as a forward-facing step with a height H equal to the hub height of the miniature turbine (i.e., 12.5 cm). The width of the model is 2.5 m and its length varies between 3 and 3.5 m along the center of the span in different cases. It is to be noted that the ratio of length L and width W of the forward-facing step to its height H are high enough such that the flow separation and reattachment from the leading edge are independent from the dimensions of the step. The reattachment length of the separated flow from the leading edge is known to become independent from the geometrical dimensions for $L/H > 4$, and for flow direction perpendicular to the leading edge $W/H > 9$ yields a two-dimensional flow [50,56]. As the incoming wind direction is fixed in the wind tunnel, the leading edge of the forward-facing step is yawed at different angles to simulate the effect of changing wind direction. Five different wind directions are simulated: $\theta = \{0^\circ, 15^\circ, 30^\circ, 45^\circ, -45^\circ\}$, where 0° represents the wind direction perpendicular to the leading edge of the cliff. The negative angle is simulated to investigate if the rotational direction of the turbine relative to the incoming wind direction can have an impact on its wake. A positive wind direction corresponds to a counterclockwise yaw of the cliff edge when viewed from the top, whereas a clockwise yaw refers to a negative wind direction. The coordinate system is defined in Fig. 1. The turbine is placed $D/\cos(\theta)$ from the leading edge of the cliff along the centerline. This is done considering that in reality, with increasing wind direction, the wind will travel a longer distance on the cliff to reach the turbine. The resulting distance d from the leading edge along the centerline is 15, 15.5, 17.3, and 21.2 cm for wind directions 0°, 15°, 30°, and $\pm 45^\circ$, respectively. To account for the wind veering effect caused by the interaction of incoming flow with the yawed leading edge of the cliff, the wind turbine is aligned with the local wind direction at the turbine hub height. This is done in consideration with the fact that for commercial wind turbines, the wind

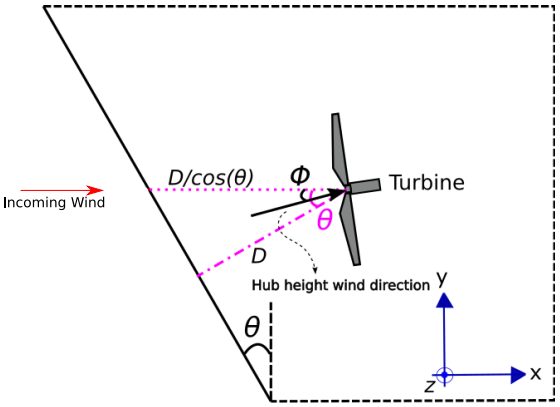

FIG. 1. A sketch of the directional and angular conventions (not to scale). The black arrow shows the local wind direction at the turbine hub height, θ denotes the wind direction relative to the yaw of the turbine, ϕ denotes wind veer, D is the rotor diameter, and z is positive away from the surface.

vane mounted on the nacelle is used to align the turbine with the incoming flow. The wind veer ϕ is extracted from the base flow data at the turbine hub location: $\phi = \tan^{-1}(V/U) = \{0^\circ, 4^\circ, 7^\circ, \pm 8.5^\circ\}$ for wind directions $\theta = \{0^\circ, 15^\circ, 30^\circ, \pm 45^\circ\}$, respectively. Figure 1 shows a sketch of the directional and angular conventions used in the study.

A stereoscopic particle-image velocimetry (S-PIV) system is used to obtain high spatial resolution cross-stream (yz-plane) flow measurements on the cliff. The S-PIV system comprises two 16-bit sCMOS cameras (2560 × 2160 pixels) with 50-mm objectives and mounted on Scheimpflug adapters to correct the camera focus onto the measurement plane. The camera aperture is fixed at $f/2.8$ with f being the focal length of the objective (i.e., 50 mm). An angle of 45° is kept between the two cameras and the size of the field of view (FOV) is 4D × 3D at a spatial resolution of about $0.016D$. The field of view is illuminated with a double-pulsed Nd:YAG laser at a wavelength of 532 nm. Following Zong and Porté-Agel [57], the thickness of the laser sheet is kept at 10 mm to minimize the loss of particle pairs due to out-of-plane motion. Measurements are acquired at a sampling rate of 10 Hz and 1000 instantaneous fields are used to obtain time-averaged flow statistics. A programmable timing unit (LaVision, PTU-v9) is used to synchronize the cameras and the laser. Olive oil droplets of several microns in diameter are generated using an in-house atomizer array and injected into the wind tunnel through a slot on the floor close to the inlet of the test section. Both cameras and the laser optics used to expand the laser beam into a sheet are mounted on synchronized high-precision motorized traversing systems (ZABER X-LRT) to facilitate cross-stream measurements at different downstream positions. For flow measurements without the turbine (base flow), measurements are taken from the prospective turbine location until eight rotor diameters downstream, whereas for the turbine wake flow, measurements are taken from 1.5 rotor diameters behind the turbine until eight rotor diameters. The streamwise interval between measurement planes is 0.25 rotor diameter for downstream distances up to five rotor diameters, whereas it is 0.5 rotor diameter for downstream distances greater than five rotor diameters. Following this procedure, 27 FOVs in the base flow and 21 FOVs in the wake flow are captured for each wind direction, resulting in a total of 240 FOVs. In a few FOVs, due to the reflection from the turbine, some noise in the turbulence quantities was observed. This was identified by the unphysically large magnitude or unphysical flow patterns compared to the neighboring flow. Such regions of noise are cropped from the data as mentioned in the description of certain figures. Pressure measurements were not performed in the study, due to which the effect of wind direction on the pressure distribution over the cliff cannot be directly quantified.

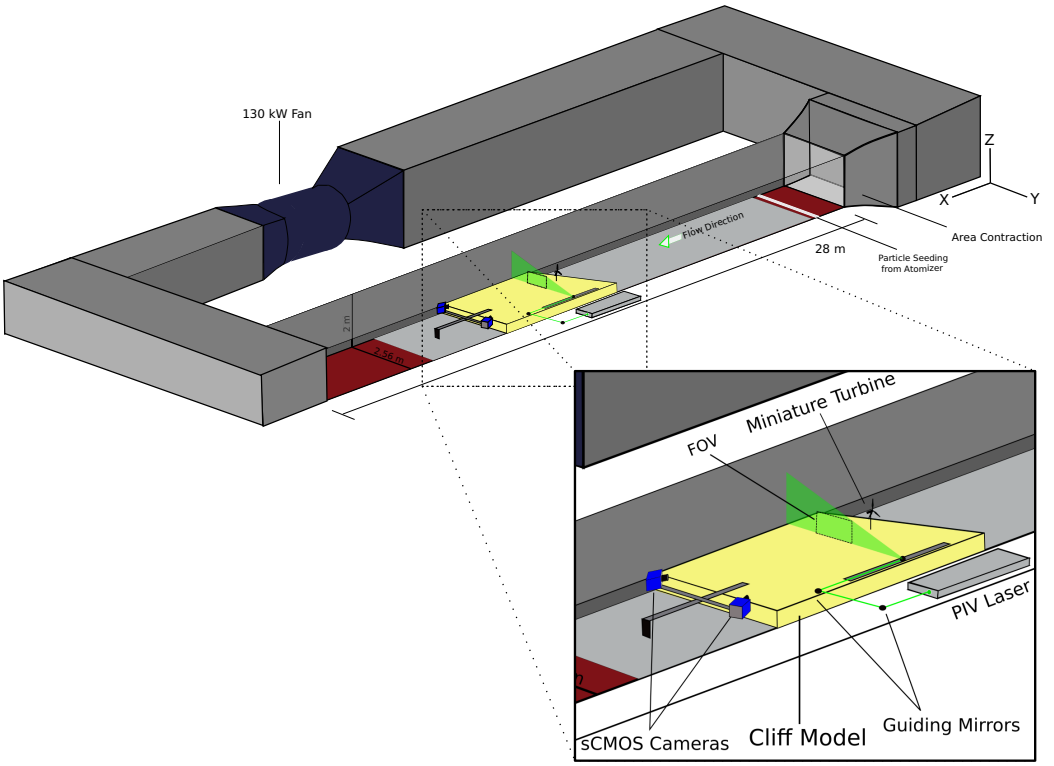

FIG. 2. A schematic of the experimental setup in the wind tunnel.

The image postprocessing is performed in double pass reducing size interrogation windows of 64×64 pixels and 32×32 pixels with a 75% overlap between neighboring windows. A universal outlier detection method is used to filter any bad vectors from the PIV data. The maximum uncertainty in mean velocity is estimated to be around 0.05 ms^{-1} using a correlation statistics approach [58]. A schematic sketch of the experimental setup is shown in Fig. 2.

The performance of the turbine on the cliff is also characterized. The power and thrust coefficients of the turbine are measured and plotted in Fig. 3 for different wind directions as a function of tip speed ratio. The mean power P generated by the turbine is measured by multiplying the torque

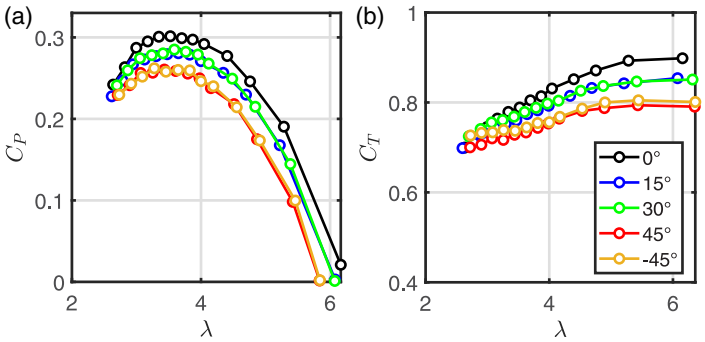

FIG. 3. (a) Power coefficient and (b) thrust coefficient of the turbine on the cliff for different wind directions as a function of tip speed ratio.

generated by the motor Q with its rotational speed Ω, where the generated torque is estimated by multiplying the generated current I with the torque constant K of the motor and adding the frictional torque Q_f of the motor. For more details on power measurement, the reader is referred to [55]. The power coefficient C_p is then computed as

$$C_p = \frac{P}{\frac{1}{2}\rho A U_d^3} = \frac{Q\Omega}{\frac{1}{2}\rho A U_d^3}, \tag{1}$$

where ρ is the air density, A is the rotor area, and U_d is the rotor-averaged velocity accounting for the effect of wind shear and veer on the available power to the wind turbine. Following Saint-Drenan *et al.* [59], the effect of wind shear is accounted for by computing a rotor-averaged velocity, and the effect of wind veer is quantified by the difference in wind direction with height with respect to the wind direction at the hub height. The rotor-averaged velocity is given by

$$U_d = \frac{1}{A}\int_{z1}^{z2}\int_{y1}^{y2} U(y,z)\cos[\Delta\phi(y,z)]dy\,dz, \tag{2}$$

where $U(y,z)$ is the streamwise velocity at each PIV grid point, $\cos[\Delta\phi(y,z)]$ quantifies the effect of wind veer, and dy, dz are the grid resolution of PIV measurements. The limits of integration are employed such that $y^2 + z^2 \leqslant R^2$, where R is the rotor radius. The rotor-averaged velocity is $U_d = \{4.6, 4.52, 4.4, 4.22, 4.29\}$ ms^{-1} for wind directions $\theta = \{0^\circ, 15^\circ, 30^\circ, 45^\circ, -45^\circ\}$, respectively. A maximum power coefficient C_p of 0.30 is observed for the 0° wind direction, which decreases with the increase in the wind direction. The maximum C_p is observed at a tip speed ratio λ of around 3.5, which is used to operate the turbine for flow measurements. It is to be noted that the tip speed ratio is varied by changing the rotor rotational speed while keeping the incoming wind at a constant value.

The thrust force T experienced by the turbine rotor is measured using a multiaxis strain gauge sensor (model ATI-nano-17Ti). The thrust coefficient C_T is computed as

$$C_T = \frac{T}{\frac{1}{2}\rho A U_d^2}. \tag{3}$$

The thrust coefficient shows a value in the range of 0.774–0.788 for the 0°, 15°, and 30° wind directions, whereas it shows a value of around 0.73 for the ±45° wind direction cases. As the thrust coefficient for the ±45° cases is smaller than the rest of the cases, the effect of wind direction will be coupled with the effect of the reduced thrust coefficient in these cases. The thrust coefficient C_T measured here is comparable to that of real-scale commercial wind turbines. It can be noted that even though the C_P values for the ±45° cases overlap for the whole range of tip speed ratio, the C_T values are slightly lower for the 45° case at low tip speed ratios. This can be likely due to some uncertainty in the force measurements. The hub height velocity U_h is $\{4.56, 4.45, 4.4, 4.15, 4.25\}$ ms^{-1} for wind directions $\theta = \{0^\circ, 15^\circ, 30^\circ, 45^\circ, -45^\circ\}$, respectively. The hub height velocity for each case is used to normalize all flow quantities in the respective cases.

The turbulent boundary layer upstream of the cliff is measured using a two-dimensional, two-component particle-image velocimetry system with a single sCMOS camera. Figure 4 shows the normalized averaged streamwise velocity U/U_h and streamwise turbulence intensity $I_u = \sigma_u/U_h$ in the upstream boundary-layer flow with σ_u as the standard deviation in the streamwise velocity. A power-law fit according to $U = U_h(\frac{z}{z_h})^n$ is also shown in Fig. 4(a), which yields an exponent n equal to 0.17. The boundary-layer height is estimated to be around 36 cm, and the streamwise turbulence intensity at the height of the cliff is 7.3%. A logarithmic fit according to $U = \frac{u_*}{\kappa}\ln(\frac{z}{z_0})$ is done on the lowest 15% of the boundary layer, which corresponds roughly to the height of the surface layer. Here, u_* is the friction velocity, which is estimated to be 0.17 ms^{-1}, κ is the von Kármán constant assumed to be 0.41, and z_0 is the aerodynamic roughness length estimated to be 0.04 mm. The logarithmic fit is shown in Fig. 4(c).

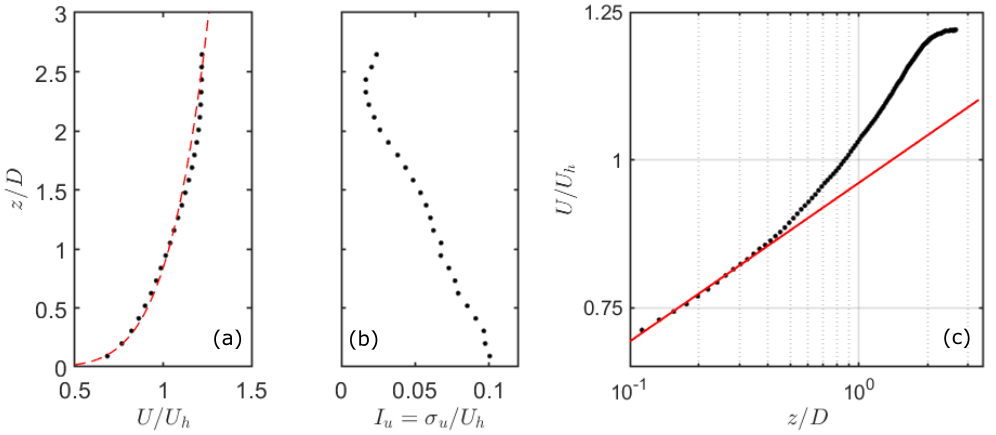

FIG. 4. Upstream boundary-layer profile: (a) normalized averaged streamwise velocity with a power-law fit shown with a red dashed line and (b) streamwise turbulence intensity and (c) normalized averaged streamwise velocity in logarithmic coordinates with a logarithmic law fit in a red line.

III. RESULTS

In this section, we present the results from the experiments. First, we discuss the flow over the cliff under different incoming wind directions without any wind turbine (termed as base flow). Understanding how wind direction affects the flow over a forward-facing step is important from a fundamental perspective. Following the base flow, we analyze the wake flow, which mainly deals with investigating the interaction between the base flow and the wake of the wind turbine sited on the cliff. It is to be noted that averaging in the current work refers to time averaging, unless otherwise mentioned.

A. Base flow

For wind directions perpendicular to the leading edge of the FFS, a flow separation occurs from the leading edge with a recirculation. This flow separation and subsequent reattachment has been found to depend on many factors such as the Reynolds number, ratio of boundary layer height to step height, and incoming turbulence level [47,60]. Here we show how the change in wind direction affects the streamwise flow separation from the leading edge. Figure 5 shows the contours of normalized averaged streamwise velocity in the base flow. For $\theta = 0^\circ$, flow separation near the leading edge is observed. The flow reattaches with the surface at about two rotor diameters downstream from the leading edge. For $\theta = 15^\circ$, streamwise recirculation (marked by the presence of negative streamwise velocity) is present and stronger near the leading edge in the spanwise direction. A spatial heterogeneity in the spanwise direction also starts to develop in the flow. For wind directions higher than 15°, no streamwise recirculation is observed. The spanwise heterogeneity is also observed to increase with an increase in the wind direction. The streamwise velocity is lower on the side of the span closer to the leading edge at larger downstream distances.

To investigate the spanwise flow induced by the FFS leading edge, we plot contours of the normalized averaged spanwise velocity along with the streamlines of the cross-stream velocity components in Fig. 6. For the wind direction perpendicular to the leading edge, the spanwise velocity is very to close to zero over the FFS, indicating a two-dimensional flow. The streamlines show a vertical velocity, which is induced by the cliff leading edge. With the increase in the wind direction, the yawed leading edge of the step induces a spanwise velocity. This spanwise velocity along with the vertical velocity component leads to the formation of a spanwise recirculation close to the leading edge. The strength of the spanwise recirculation increases with the increase in wind

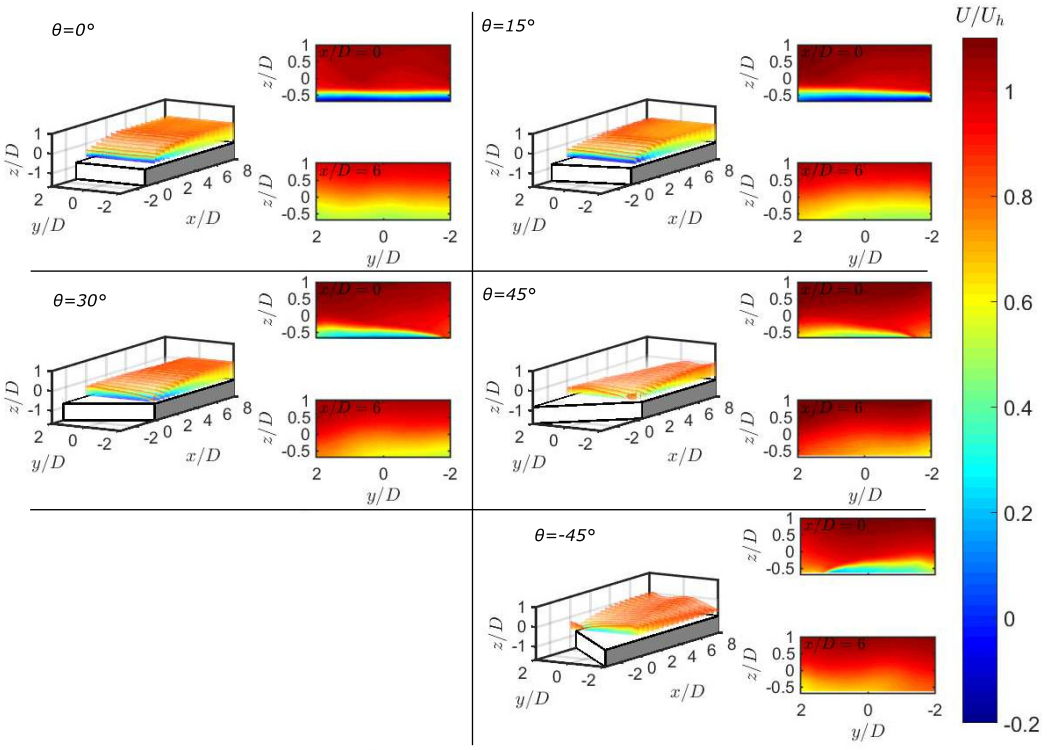

FIG. 5. Contours of the normalized averaged streamwise velocity in the base flow. The three-dimensional plot shows the development of the shear layer from the cliff leading edge. The three-dimensional contours show steramwise velocity in the range $U/U_h < 0.85$. The color bar applies to all contours shown in the figure.

direction. For wind directions above 15°, as the streamwise recirculation disappears, the streamwise velocity advects the spanwise recirculation in the streamwise direction, leading to the helical vortex formation. Further downstream from the leading edge, the spanwise velocity reduces in magnitude, but it still maintains the directional preference dictated by the spanwise recirculation and gives rise to a wind veering effect.

We now focus on turbulence characteristics in the base flow. Figure 7 shows the contours of the normalized turbulence kinetic energy TKE $= \frac{\overline{u'^2}+\overline{v'^2}+\overline{w'^2}}{2}$, where u', v', and w' are the fluctuating components of the streamwise, spanwise, and vertical velocity, respectively. The turbulence kinetic energy over the FFS is contributed by that in the incoming flow and that generated by the shear induced by the separating flow from the leading edge. The second mechanism usually contributes more than the first one as high shear close to the leading edge generates most of the turbulence over the FFS. For the wind direction perpendicular to the leading edge of the FFS, high TKE is observed close to the edge which decreases further downstream due to the expansion of the shear layer developed from the leading edge. Interestingly, the normalized TKE increases in magnitude for $\theta = 15^\circ$ compared to $\theta = 0^\circ$. However, for wind directions greater than 15°, a decrease in the magnitude of normalized TKE is found. A similar observation was made by Rowcroft *et al.* [52], who found that the turbulence intensity gain over the FFS maximized at $\theta = 20^\circ$; however, no explanation was provided in their work. In the following, we provide a physical explanation for the TKE trend.

To understand the TKE trends observed in Fig. 7, we look into the primary mechanism responsible for turbulence generation. In a turbulent flow, the turbulence kinetic energy is extracted from

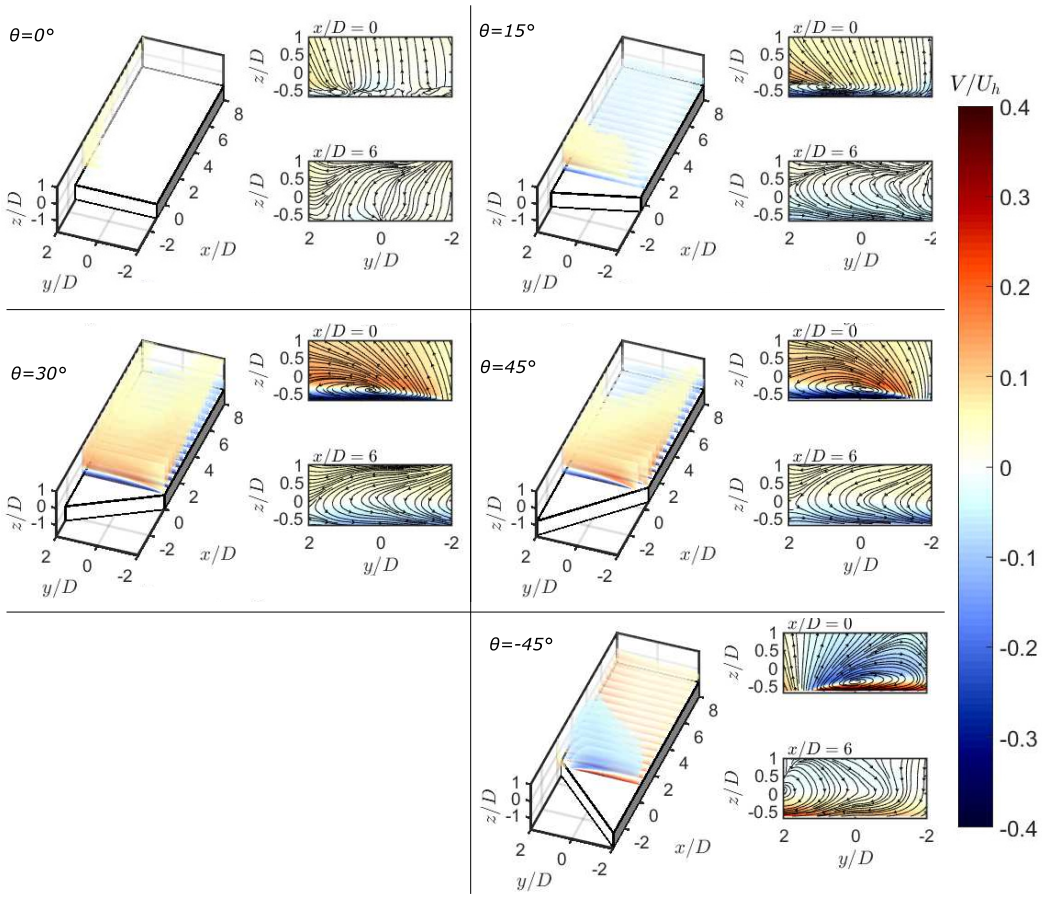

FIG. 6. Contours of the normalized averaged spanwise velocity in the base flow. Streamlines of the cross-stream velocity profiles are overlaid on the two-dimensional contour plot. The three-dimensional contours show spanwise velocity in the range $-0.04 > V/U_h > 0.04$. The color bar applies to all contours shown in the figure.

the mean flow. Figure 8 shows contours of the normalized turbulence production via shear in the mean flow. Total production, as well as the individual contribution of shear in averaged streamwise velocity and vertical shear in averaged spanwise velocity are shown.

The normalized total production of TKE shows a similar trend to that of TKE, with a decrease in magnitude for $\theta > 15^\circ$ [Fig. 8(a)]. The contribution of shear in averaged streamwise velocity also shows a similar trend in Fig. 8(b). The decrease in the contribution of shear in averaged streamwise velocity can be associated with the streamwise recirculation in the flow. As shown earlier, the streamwise recirculation is observed for $\theta = \{0^\circ, 15^\circ\}$, whereas it disappears for higher wind directions. As the streamwise recirculation disappears, the shear in the averaged streamwise velocity decreases, which eventually leads to lesser turbulence production. With increasing wind direction, however, a spanwise recirculation is induced. To understand its role in turbulence production, we plot contours of the normalized turbulence production due to vertical shear in averaged spanwise velocity in Fig. 8(c). As expected, the contribution from this term to turbulence production increases with increasing wind direction. However, the magnitude of this term is almost three times less than that of the turbulence production due to averaged streamwise velocity. Therefore, the increase in the contribution of vertical shear in spanwise velocity towards turbulence production cannot compensate for the decrease in turbulence production due to shear in streamwise velocity, and an overall decrease

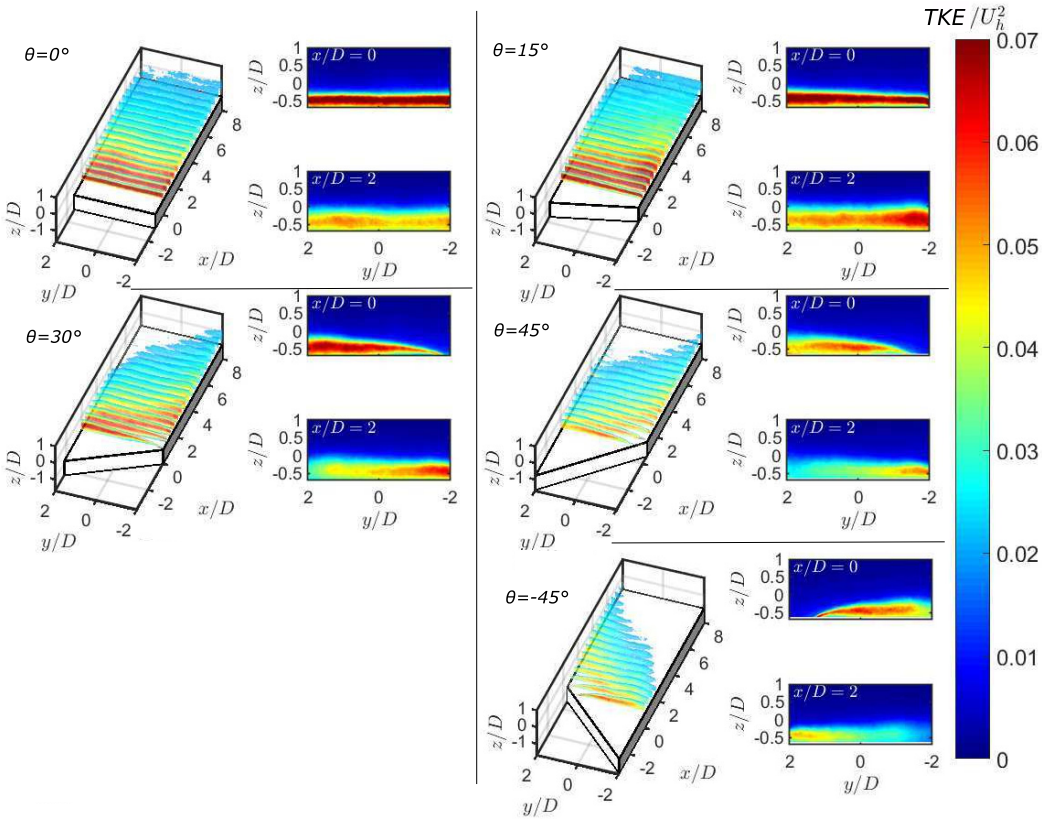

FIG. 7. Contours of the normalized turbulence kinetic energy in the base flow. The three-dimensional contours show turbulence kinetic energy in the range $\mathrm{TKE}/U_h^2 > 0.02$. The color bar applies to all contours shown in the figure.

in turbulence production is observed for wind directions above 15°. It is to be noted, however, that for wind directions above 15°, recirculation in spanwise velocity still plays a major role in overall turbulence production.

B. Wake flow

We now turn our attention to the wake of a wind turbine sited on a cliff under different incoming wind directions. Our primary focus is to understand how the complicated base flow generated by the cliff interacts with the wake of the wind turbine and affect its characteristics.

1. Time-averaged flow characteristics

Figure 9 shows the contours of the normalized averaged streamwise velocity in the turbine wake for different incoming wind directions. For $\theta = 0°$, a low velocity in the turbine wake, along with a flow speedup outside the wake can be identified. The wake shows a symmetrical distribution in the spanwise direction across the centerline of the turbine. With the increase in the wind direction, the shape of the wake is observed to change due to the interaction with the base flow. For $\theta = 15°$, the streamwise velocity shows an asymmetrical distribution across the centerline of the rotor, with a high-speed region on the left side of the rotor projected area. This asymmetry in the streamwise velocity is observed to increase with the streamwise distance and can be observed in the far wake as well. For $\theta = 30°$, a similar asymmetrical distribution is observed in the near wake,

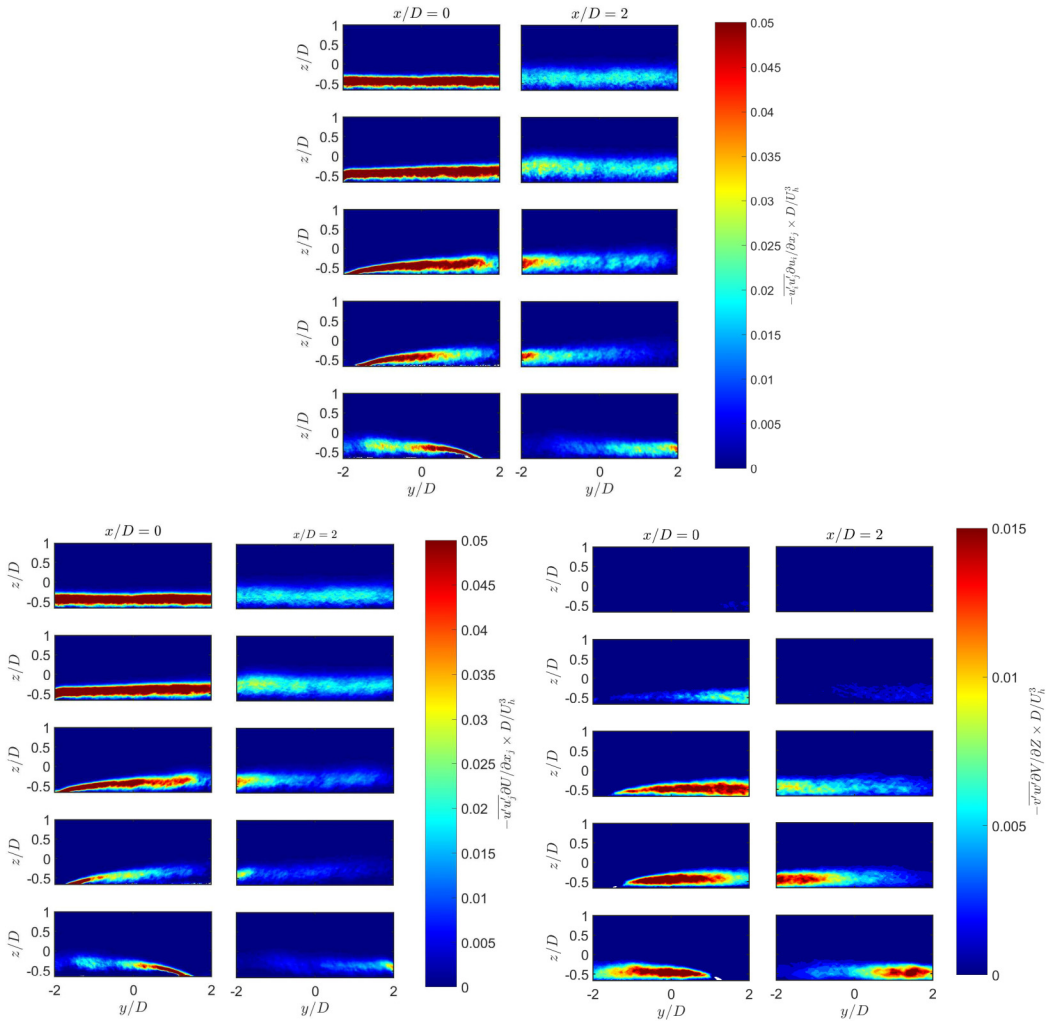

FIG. 8. Contours of the normalized turbulence production via shear: (a) total production, (b) production due to shear in averaged streamwise velocity, and (c) production due to vertical shear in averaged spanwise velocity. From top to bottom: 0°, 15°, 30°, 45°, and −45°.

with a highspeed region on the left side of the turbine, respectively. In the far wake, however, the streamwise velocity shows a relatively symmetrical profile. Within the rotor-projected area in the near wake, the streamwise velocity minimum is observed to be shifted away from the rotor center position. In the 0° wind direction, the low-speed region outside the wake is the flow from the leading edge of the cliff unaffected by the presence of the turbine. For higher wind directions, however, the interaction between the wake and the base flow is observed until $|y/D| = 2$. For $\theta = 45°$, the wake shape within the rotor-projected area is observed to be affected by the base flow, with a deflection from the rotor centerline close to the surface. For $\theta = -45°$, a similar behavior is observed with an opposite orientation.

The magnitude of the normalized averaged streamwise velocity is also observed to be affected by the incoming wind direction (see Fig. 9). The wind direction perpendicular to the cliff leading edge shows the lowest normalized averaged streamwise velocity in the turbine wake, where the values of U/U_h are observed to increase with the increase in the wind direction. This can be related to the

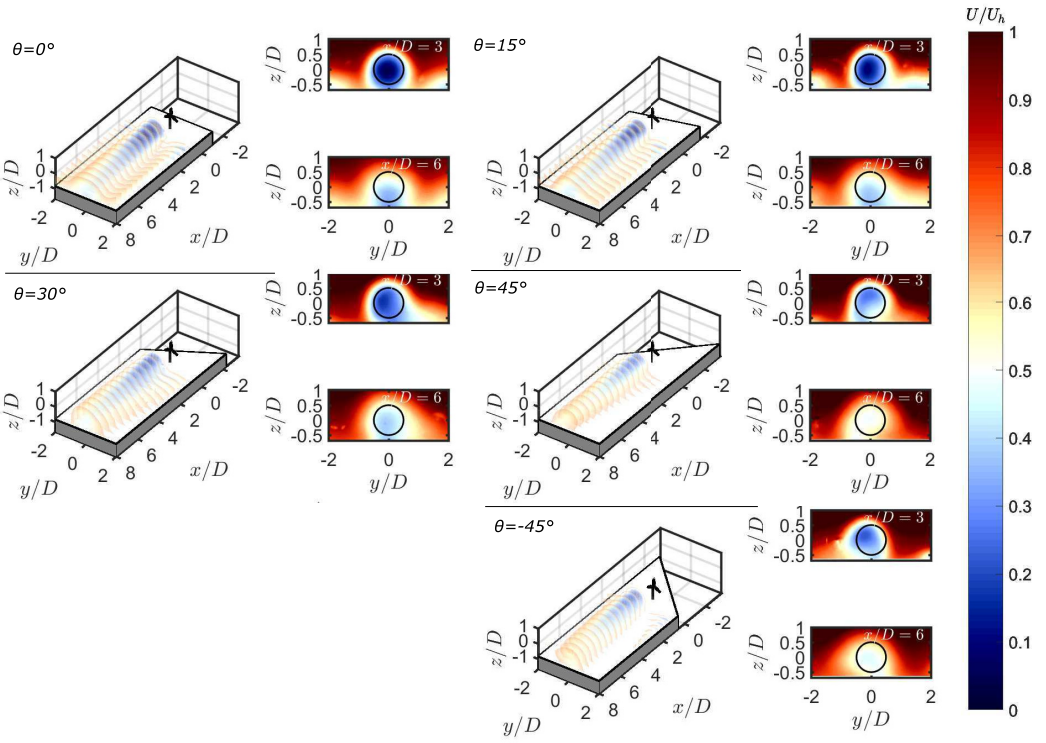

FIG. 9. Contours of the normalized averaged streamwise velocity in the turbine wake. The three-dimensional plot shows streamwise velocity in the range of $U/U_h < 0.7$. The color bar applies to all contours shown in the figure. The black circles in two-dimensional contours show the rotor-projected area.

normalized averaged streamwise velocity in the base flow, which shows a similar trend with wind direction. The increase in the magnitude of U/U_h with the wind direction can be due to the decrease in the shear in the averaged streamwise velocity caused by the disappearance of the streamwise recirculation in the base flow. Moreover, the thrust coefficient of the turbine also shows a decrease with the increase in the wind direction (approximately 1.8% and 7.3% between the 0° and 30° cases, and 0° and 45° cases, respectively). This could also have an effect on the magnitude of the normalized averaged streamwise velocity. For $\theta \leqslant 30^\circ$, however, this effect is expected to be very small. For $\theta = \pm 45^\circ$, the effect of change in the wind direction and the thrust coefficient are coupled together, and result in an increase in the magnitude of the normalized streamwise velocity in the wake.

The spanwise and vertical velocity induced by the base flow in nonzero wind directions affect the wake of the turbine. Figure 10 shows the contours of the normalized averaged spanwise velocity induced by the interaction between the spanwise recirculation in the base flow and the turbine wake. For $\theta = 0^\circ$, the normalized averaged spanwise velocity is the smallest out of all the cases and contributed solely by the turbine wake due to an almost zero spanwise velocity in the base flow. With the increase in the wind direction, the normalized averaged spanwise velocity outside the rotor-projected area gets stronger. For $\theta = 15^\circ$, the negative spanwise velocity close to the surface in the base flow is relatively small. For wind directions $\theta > 15^\circ$, however, a very strong negative spanwise velocity can be observed close to the surface on the right of the rotor-projected area. This strong spanwise velocity is responsible for the change in streamwise velocity distribution from a skewed shape towards the right of the rotor in $\theta = 15^\circ$ to a relatively symmetric one in $\theta = 30^\circ$ to the one shifted towards the left of the rotor in $\theta = 45^\circ$ in the far wake. The difference in the

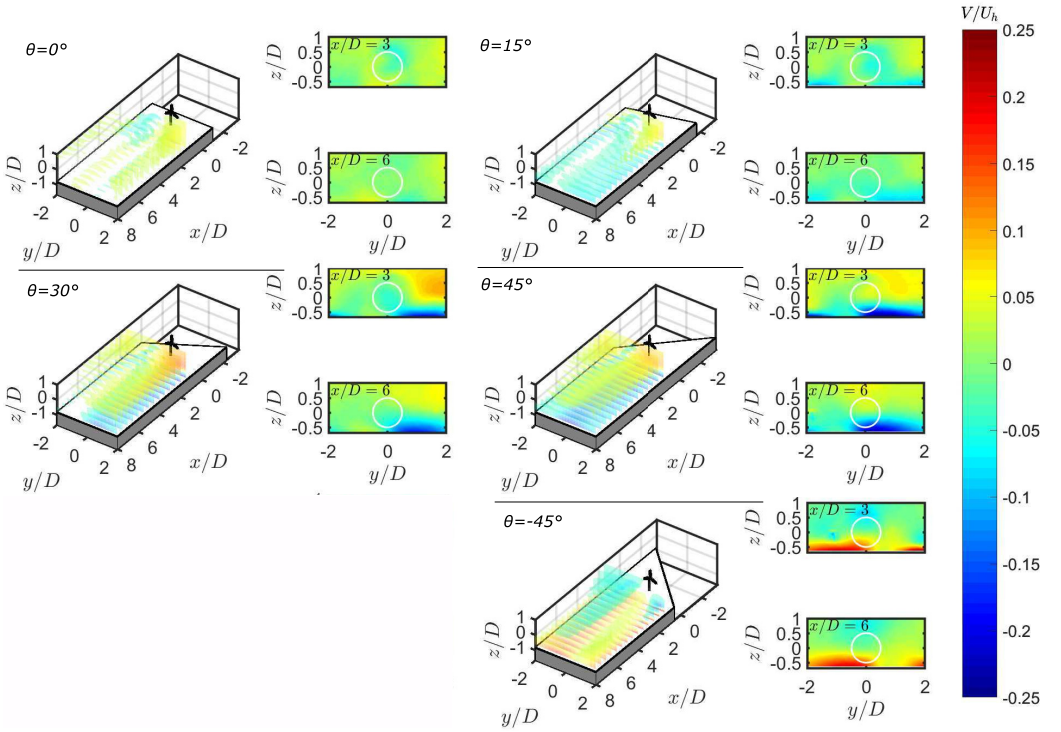

FIG. 10. Contours of the normalized averaged spanwise velocity in the turbine wake. The three-dimensional plot shows spanwise velocity in the range of $-0.025 > V/U_h > 0.025$. The color bar applies to all contours shown in the figure. The white circles in two-dimensional contours show the rotor-projected area.

spanwise velocity between the positive and negative 45° wind direction cases can also be observed. In the case of 45°, a negative spanwise velocity near the surface and positive spanwise velocity on one side of the rotor away from the surface can be observed. For the −45° wind direction, on the other hand, a positive velocity near the surface is observed, and a negative one away from it. This is due to the formation of a vortex on one side of the rotor, which depends on the direction of the base flow. The origin of this spanwise velocity and its role in determining the wake shape will be discussed in detail later.

To characterize the difference in the turbine wake compared to the base flow and isolate the influence of the turbine on the wake flow, we compute the averaged streamwise velocity deficit $\Delta U(x, y, z) = U_b(x, y, z) - U_w(x, y, z)$, where U_b is the averaged streamwise velocity in the base flow and U_w is the averaged streamwise velocity in the wake flow. Figure 11 shows the contours of the normalized averaged streamwise velocity deficit in the turbine wake for different wind directions. A black contour representing $0.5\Delta U_{\max}(x)/U_h$ is also included to distinguish the shape of the wake between different cases. Similar to the streamwise velocity contours, the shape of the wake velocity deficit is observed to be affected by the wind direction, with a symmetric distribution in the cross-stream plane across the turbine centerline for $\theta = 0°$. For the higher wind directions, two factors play a key role in determining the wake shape: the lateral velocity component that develops in the base flow and the flow speedup at the spanwise boundary of the wake close to the surface. For $\theta = 0°$, the flow speedup close to the surface outside the wake deficit is also symmetric. As explained by Dar and Porté-Agel [44], this speedup occurs as the presence of the turbine suppresses the development of the separated flow from the cliff leading edge, and therefore, reduces the shear

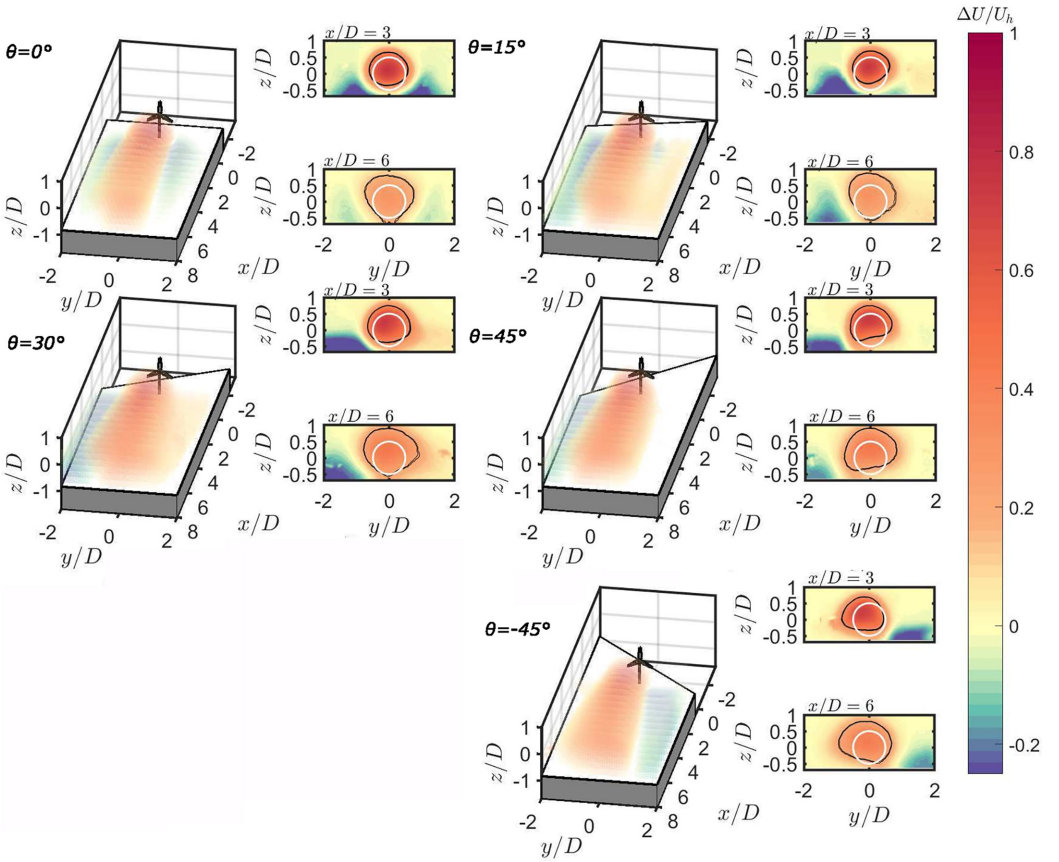

FIG. 11. Contours of the normalized averaged streamwise velocity deficit in the turbine wake. The three-dimensional plot shows streamwise velocity deficit in the range of $-0.04 > \Delta U/U_h > 0.04$. The color bar applies to all contours shown in the figure. The black contour lines and the white circles in two-dimensional contours show $0.5\Delta U_{\max}(x)/U_h$ and the rotor-projected area, respectively.

in the surrounding flow which leads to the speedup observed here. For higher wind directions, on the other hand, the speedup is only observed on one side of the rotor, the magnitude of which is much higher than that for $\theta = 0^\circ$. The expansion of the wake velocity deficit in the cross-stream plane is also observed to be affected by the wind direction, which leads to a difference in the recovery of the maximum streamwise velocity deficit due to momentum conservation, which will be discussed later in the article.

For now, we turn our focus towards understanding the differences in the shape of the wake for different incoming wind directions. At the moment, two questions remain: how does the spanwise recirculation for higher wind directions interact with the wind turbine wake, and what gives rise to the flow speedup observed on one side of the rotor for higher wind directions? To answer these questions, we plot the contours of the normalized averaged streamwise vorticity in the flow in Fig. 12. For $\theta = 0^\circ$, the vorticity in the near wake is dominated by the tip and hub vortices shed by the turbine, whereas in the far wake, a counter-rotating vortex pair (CVP) is observed to develop close to the surface. As explained by [44], the vertical velocity experienced by the turbine from the cliff leading edge leads to the formation of the CVP with a mechanism similar to how the lateral velocity induced by a yawed turbine gives rise to a CVP in the wake. For nonzero wind directions, the vorticity distribution is affected by the spanwise vorticity in the base flow. With the increase

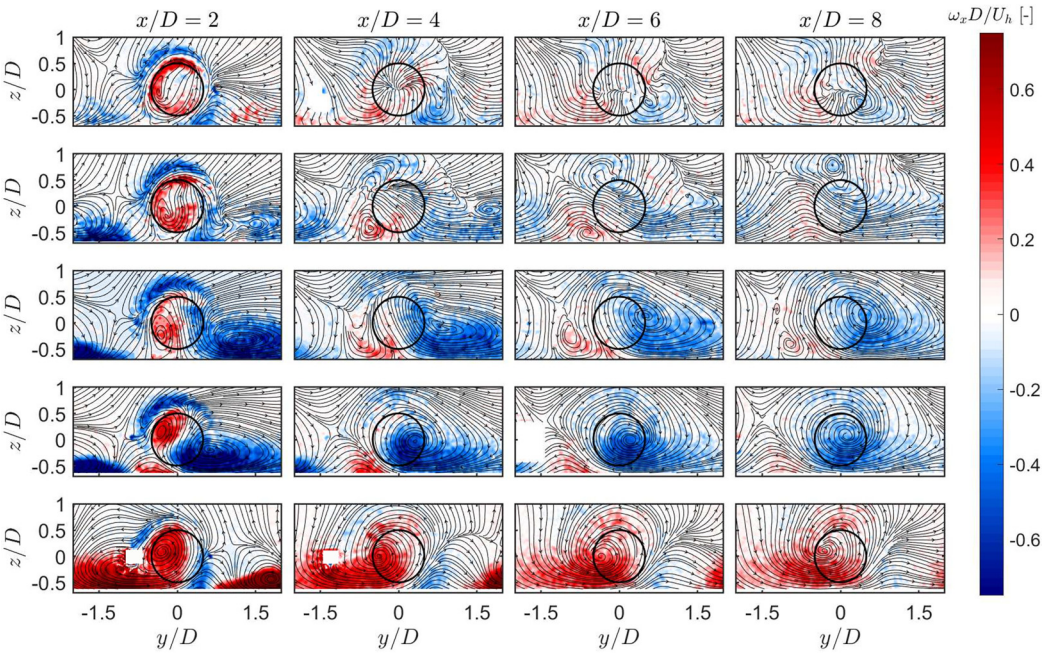

FIG. 12. Contours of the normalized averaged streamwise vorticity in the turbine wake. Streamlines based on cross-stream velocity components are overlaid. The black circles show the rotor-projected area. From top to bottom: $\theta = 0^\circ$, 15°, 30°, 45°, -45°. The white rectangles in some panels crop the noisy data from PIV.

in the wind direction, one leg of the CVP is observed to grow stronger compared to the other and dominates the flow. The leg of the CVP dominating the flow is found to be dependent on the direction of the spanwise recirculation. This is likely due to the development of high shear around the rotor periphery in the near wake which restricts the base flow spanwise velocity on one side of the rotor in higher wind directions.

To explain the flow speedup outside the wake, we focus on the streamlines in the cross-stream planes. The streamlines show some interesting flow structures, the most notable of which is the formation of a saddle point on one side of the rotor in the near wake of the turbine. This saddle point divides the wake flow from the outer base flow, creating two distinct regions of flow and leads to the flow speedup observed on the side of the rotor. The vertical position of the saddle point is observed to get close to the surface with the increase in the wind direction, which restricts the vertical extent of the flow speedup close to the surface. The position of the saddle point is found to be dependent on the wind direction, as it appears on the left of the turbine center for the positive wind directions and on the right for the negative one. For $\theta = 0^\circ$, the saddle point is replaced by a stable node at the rotor center in the turbine far wake. The formation of this stable node leads to an enhanced entrainment of flow from outside into the wake and to the development of the CVP in the far wake of the turbine.

For higher wind directions, the cross-stream flow structures are rather complex and dependent on the strength of the spanwise recirculation in the base flow. For $\theta = 15^\circ$, a spanwise velocity is induced by the yawed cliff edge; however, the spanwise recirculation is relatively small. In the turbine near wake, a small vortex is observed outside the wake on the right side of the rotor. This vortex does not merge with the tip and hub vortices developed from the rotor tips and hub. Further downstream, as the vortices shed by the turbine break down, the spanwise velocity in the base flow sweeps through the rotor-projected area. The presence of a saddle point on the other side of the rotor, however, restricts further movement of the spanwise flow velocity in the spanwise direction,

which in turn results in the roll up of the vortices and formation of a CVP with an orientation that is 90° rotated compared to one for $\theta = 0°$. The saddle point is also observed to move up and away from the turbine center with an increase in the streamwise distance, which could be related to the expansion of the wake in the cross-stream directions. As the saddle point exists throughout the far wake, the flow speedup observed on the right of the rotor does too, which leads to a stronger speedup in the far wake compared to $\theta = 0°$.

For wind directions above 15°, the spanwise recirculation in the base flow is strong enough to interact with the vortices shed by the turbine itself. For $\theta = 30°$, in the near wake, the vortex on the right side of the rotor limits the development of the hub vortex and induces a high vertical velocity within the rotor-projected area at the interface of the hub vortex and the base flow vortex. This vortex is also responsible for the shift in the position of the maximum streamwise velocity deficit away from the turbine center. Further downstream, it dominates the flow and the positive leg of the CVP observed in $\theta = 15°$ diminishes in size for $\theta = 30°$. The spanwise velocity observed in the turbine wake is induced by this vortex.

For $\theta = 45°$, a similar observation is made, where the base flow vortex is even stronger than that for $\theta = 30°$. The strong base flow vortex affects the hub vortex even more and pushes the wake towards the left side of the rotor near the surface. As the rotation of the hub and base flow vortices are opposite, they do not merge into one in the turbine near wake. In the far wake, the hub vortex breaks down, whereas the base flow vortex dominates the flow. For $\theta = -45°$, on the other hand, the hub vortex and the base flow vortex are observed to merge into one, which shifts the wake center slightly towards the left of the turbine center. In the near wake, similar to the positive wind directions, a saddle point is observed. In the far wake, however, this saddle point is replaced by an unstable node, which divides the vortex developed due to the merger of the hub and base flow vortices, and the outer base flow. In general, the shape of the wake and the flow speedup outside the wake are shown to be affected by the cross-stream flow structures like the saddle point and the CVP in all cases.

2. Turbulence characteristics

Typically, the turbulence kinetic energy is contributed by the turbulent momentum fluxes and mean flow shear [61]. For a wind turbine wake in flat terrain, the spatial distribution of turbulence kinetic energy shows a horseshoe shape with a peak around the rotor top tip level. This is due to high mean flow shear and momentum fluxes around the rotor periphery at the top. Moreover, the maximum turbulence kinetic energy and related turbulent momentum fluxes are relatively higher in the turbine wake compared to the surrounding boundary-layer flow [61,62].

Figure 13 shows the contours of the normalized turbulence kinetic energy in the turbine wake on the cliff for different wind directions. For the wind direction $\theta = 0°$, a typical horseshoe shape of high TKE is observed, along with some turbulence in the outer flow closer to the cliff leading edge due to high shear. With downstream distance, the magnitude of TKE in the turbine wake decreases due to a decrease in the mean flow shear, although the shape is preserved. As shown earlier, the mean velocity and the wake shape are highly dependent on the wind direction, due to the induction of spanwise recirculation and development of streamwise vorticity in the wake flow. This has an effect on the turbulence kinetic energy in the wake, as it affects both the shear in the mean flow as well as the distribution of the turbulent momentum fluxes. Figure 14 shows the contours of the normalized averaged lateral and vertical turbulent momentum fluxes for different incoming wind directions. The influence of the streamwise vorticity on the spatial distribution of these turbulent fluxes can be clearly observed, especially close to the turbine. High turbulence kinetic energy is observed in areas with high mean flow shear, including the rotor top periphery and the surrounding base flow closer to the cliff edge. The shape of the high TKE region around the rotor periphery is affected by the shape of the wake, where especially for high wind directions $\theta = \pm 45°$, the peak in the TKE is observed to be shifted on one side of the rotor in the far wake. In the base flow, the normalized TKE was observed to peak at $\theta = 15°$. In the wake flow, the normalized TKE is

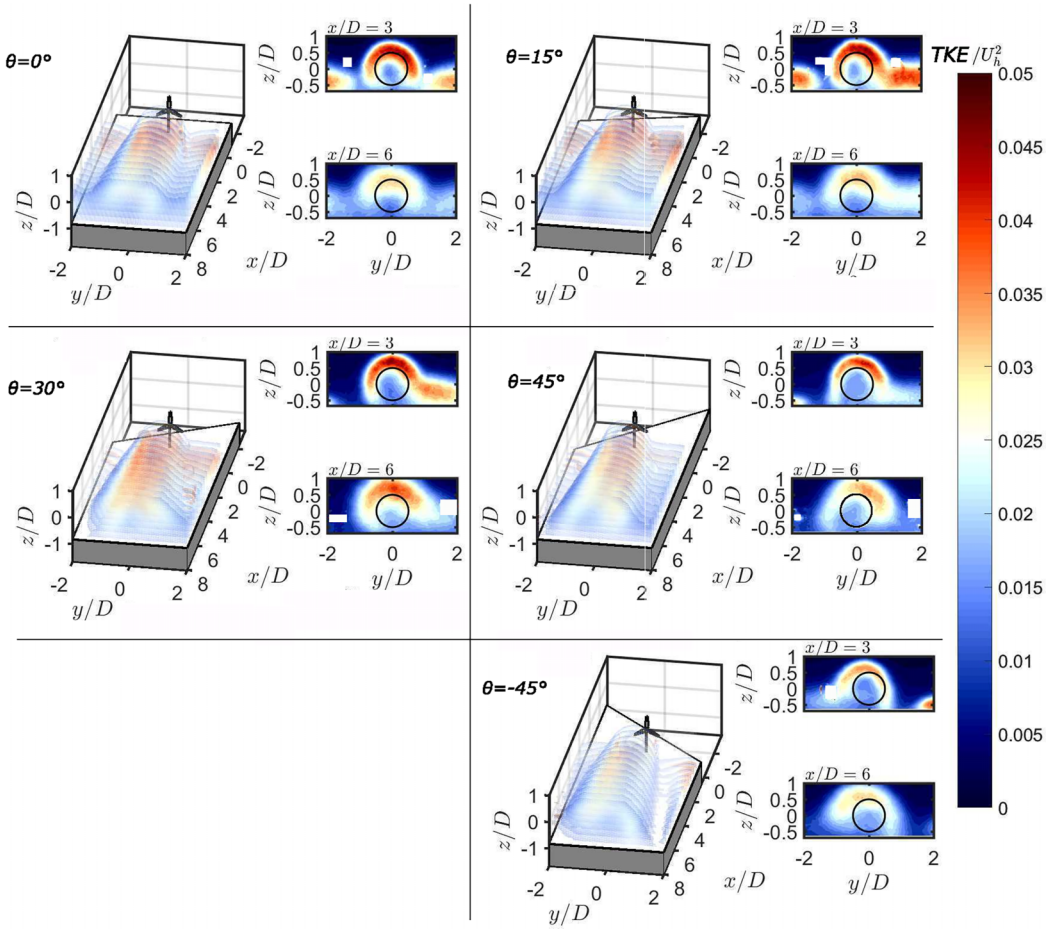

FIG. 13. Contours of the normalized turbulence kinetic energy in the turbine wake. The three-dimensional plot shows turbulence kinetic energy in the range of $\mathrm{TKE}/U_h^2 > 0.01$. The black circles in two-dimensional contours show the rotor-projected area. The white rectangles in some panels crop the noisy data from PIV.

observed to be highest for $\theta = 30^\circ$, which can be related to the highest magnitude of turbulent momentum fluxes observed for this wind direction compared to the rest of the cases, especially in the far wake (see Fig. 14).

3. Volumetric wake characterization

In order to characterize the streamwise wake velocity deficit, we perform a volumetric wake analysis following Brugger *et al.* [63]. For this purpose, a two-dimensional (2D) Gaussian fit is performed on the streamwise wake velocity deficit in the cross-stream direction at several streamwise positions. The 2D Gaussian fit is given by

$$\Delta U(y,z) = C\exp[-a(y-y_0)^2 + 2b(y-y_0)(z-z_0) + c(z-z_0)^2], \tag{4}$$

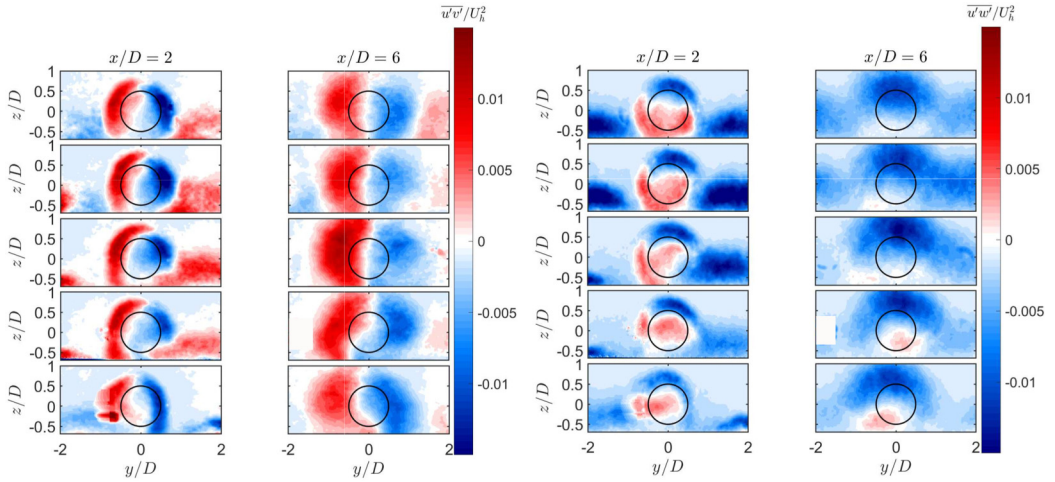

FIG. 14. Contours of the normalized averaged lateral (left) and vertical (right) momentum flux in the turbine wake for two different streamwise positions. The black circles show the rotor-projected area. From top to bottom: $\theta = 0°, 15°, 30°, 45°, -45°$. The white rectangles in some panels crop the noisy data from PIV.

where

$$a = \frac{\cos^2(\alpha - 90)}{2\sigma_y^2} + \frac{\sin^2(\alpha - 90)}{2\sigma_z^2}, \tag{5}$$

$$b = \frac{\sin[2(\alpha - 90)]}{4\sigma_y^2} + \frac{\cos[2(\alpha - 90)]}{4\sigma_z^2}, \tag{6}$$

$$c = \frac{\sin^2(\alpha - 90)}{2\sigma_y^2} + \frac{\cos^2(\alpha - 90)}{2\sigma_z^2}. \tag{7}$$

The maximum velocity deficit is represented by C; σ_y and σ_z are the standard deviations representing wake widths along the principal axes of the 2D Gaussian fit; y_0 and z_0 represent the wake center deviation from the rotor center position and α represents the tilt angle of the wake in the 2D Gaussian fit. Figure 15 shows a schematic of the 2D Gaussian fit and different

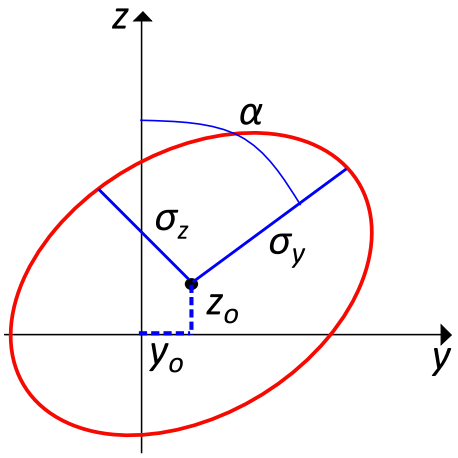

FIG. 15. Schematic of the 2D Gaussian fit.

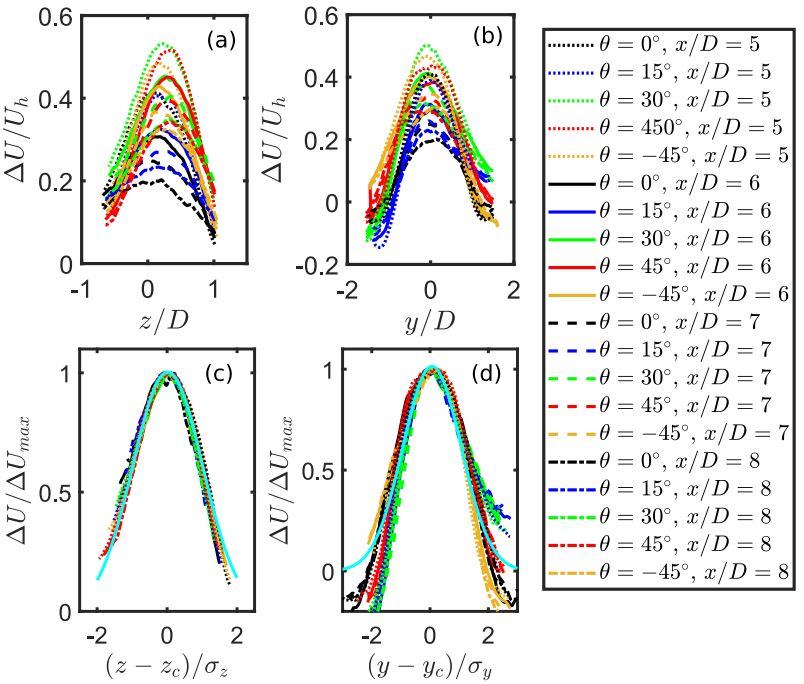

FIG. 16. Comparison of the vertical (a) and lateral (b) profiles of the normalized averaged streamwise velocity deficit in the wake flow. Vertical (c) and lateral (d) profiles of the streamwise velocity deficit normalized by the maximum velocity deficit and wake width. A Gaussian profile is overlaid in cyan color.

fitting parameters. The fit is performed with a weighted nonlinear least-squares regression, where only the positive velocity deficit is used for fitting. To initialize the fit at $x/D = 2$, starting values corresponding to $C = 4$ ms^{-1}, $\sigma_y = \sigma_z = 0.05$ m, $y_0 = z_0 = 0$ m, and $\alpha = 0°$ are used. For each subsequent streamwise position, the fitted parameters from the previous position are used for initialization.

Figures 16(a) and 16(b) show the vertical and lateral profiles of the wake velocity deficit in the far wake for all the cases. The difference in the velocity deficit between different wind direction cases can be identified. Figures 16(c) and 16(d) show the vertical and lateral profiles of the wake velocity deficit normalized by the maximum velocity deficit and wake width for all the cases. In order to assess self-similarity, the velocity deficit is normalized by its maximum value at a given streamwise location, and the vertical and lateral distances are normalized by the wake width in their respective directions. It can be observed that, for a given wind direction, all profiles in the vertical and lateral directions collapse on a single profile. There are, however, some differences between different wind directions, which are caused by the difference in the flow shear towards the wake edges and due to varying levels of flow speedup outside the wake in different cases. These differences are particularly pronounced in the lateral direction. As the Gaussian curve does not account for the flow speedup outside the wake, the lateral profiles show deviation from the Gaussian profile at the wake edges for some cases. Around the wake center, some lateral profiles show a slightly higher width than the Gaussian curve, indicating a relatively flattened wake center. This indicates that the self-similarity is relatively weak in the lateral profiles. To further analyze this, we show a comparison of the experimental wake velocity deficit with the corresponding 2D Gaussian fit in Fig. 17. The coefficient of determination between the fit and the experiments is in the range of 0.935–0.97 for different cases. Even though the wake velocity deficit is not a perfect ellipse, especially in the cases with high wind directions, as can be seen in Fig. 17, the 2D Gaussian

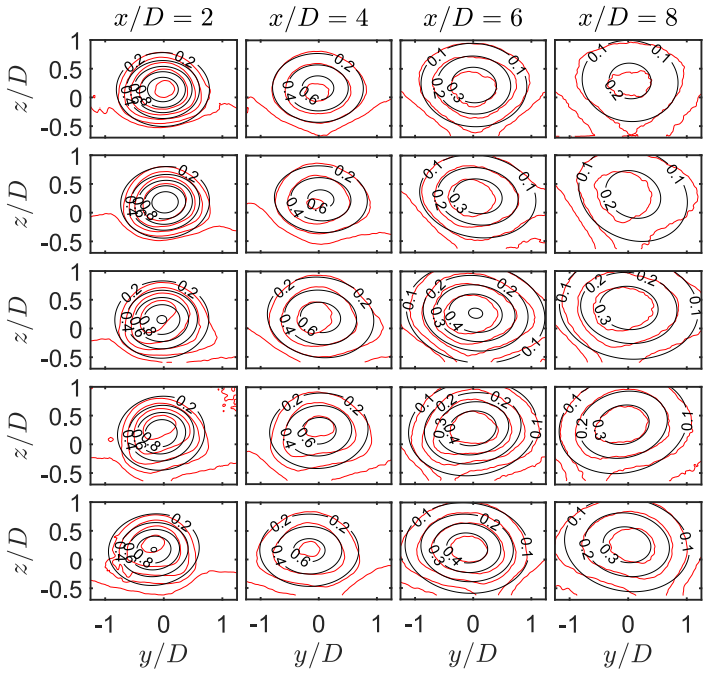

FIG. 17. Comparison of the contours of the normalized averaged streamwise wake velocity deficit between the experiments (red) and 2D Gaussian fit (black). From top to bottom: $\theta = 0°$, $15°$, $30°$, $45°$, $-45°$.

fit approximates the wake shape and magnitude reasonably well. Due to the departure from the perfect elliptical shape in some cases, the value of the coefficient of determination is slightly lower than the threshold of 0.96 defined by [63] for wakes under wind veer. However, it still presents a reasonable first approximation to determine the wake width and deviation of the mean wake center.

Some key wake characteristics are plotted and compared for different wind directions as a function of the streamwise distance in Fig. 18. The recovery of the wake center velocity deficit is quantified via the evolution of the maximum normalized averaged streamwise velocity deficit in Fig. 18(a). Closer to the turbine, the wind direction perpendicular to the cliff edge shows the highest value of $\Delta U_{\max}/U_h$ among all the cases, with values decreasing slightly with the increase in the wind direction. This can be related to the difference in the thrust coefficient observed between different wind directions shown in Fig. 3(b), and to the effect of the pressure gradient induced by the cliff leading edge on the turbine near wake. As discussed by [44], although the streamwise velocity deficit in the turbine wake is contributed solely by the turbine thrust in a flat terrain, in a complex terrain, there is an additional contribution resulting from the terrain-induced pressure gradient. As a cliff induces an adverse pressure gradient, this additional contribution results in a higher velocity deficit than without the effect of the induced pressure gradient.

Further downstream, the rate of recovery of the wake center velocity deficit is also found to be dependent on the wind direction. The wind directions $\theta = \{0°, 15°\}$ show the highest recovery rate among all the cases. For wind directions $\theta > 15°$, on the other hand, the recovery rate is observed to significantly slow down compared to the first two cases. This observation is consistent with the base flow normalized turbulence kinetic energy, which is observed to decrease for $\theta > 15°$. In addition, the induction of a spanwise velocity in the base flow also results in veering in the vertical direction and leads to the formation of complex vortical structures as illustrated earlier (see Fig. 12). This cross-stream flow development affects the expansion of the wake, which in turn can affect the recovery of the wake center velocity deficit due to momentum conservation. Figure 18(b) shows

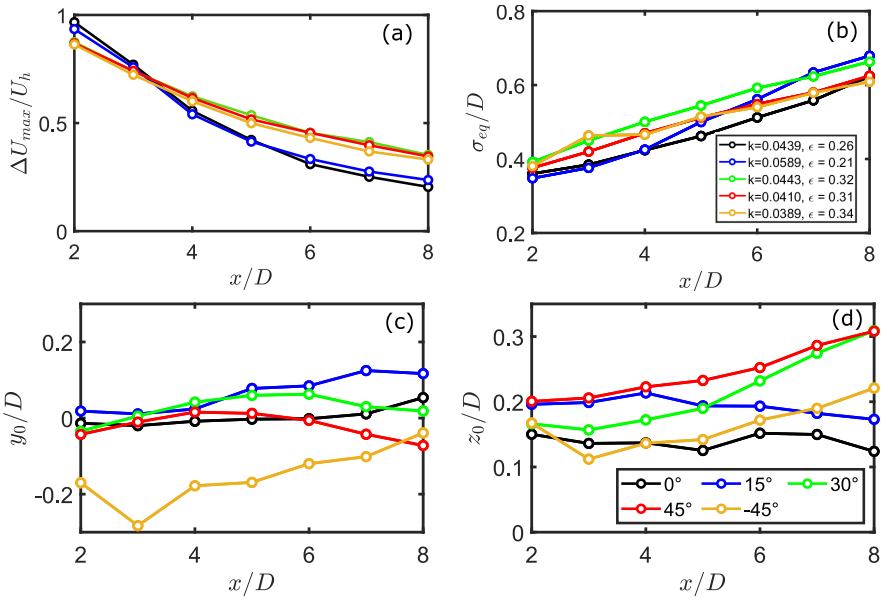

FIG. 18. (a) Maximum normalized averaged streamwise velocity deficit, (b) normalized equivalent wake width, and wake center deflection in the (c) spanwise and (d) vertical direction as a function of streamwise distance.

the normalized equivalent wake width computed as the geometrical mean of the wake widths along the principal axes of the 2D Gaussian fit ($\sigma_{\text{eq}} = \sqrt{\sigma_y \sigma_z}$). All cases show an approximately linear trend in the normalized equivalent wake width, which is consistent with earlier studies [4,44]. A linear fit according to $\sigma_{\text{eq}}/D = kx/D + \epsilon$ is performed on the normalized wake width. The resulting wake growth rate k and initial wake width ϵ values are shown in Fig. 18(b). The wake growth rate is observed to decrease for wind directions greater than 15°, which is consistent with the slower wake recovery for these cases. In addition, the initial wake width is observed to be higher for the cases with wind directions greater than 15°, which explains the higher wake width in these cases compared to the 0° one. For $\theta = 15°$, the normalized equivalent wake width is observed to be similar to that for $\theta = 0°$ at $x/D \leqslant 4$, whereas it shows a higher σ_{eq}/D at $x/D > 4$. This could be related to the formation of the CVP aligned with the saddle point as shown in Fig. 12, which stretches the wake in the vertical direction leading to a higher equivalent wake width.

The deflection of the wake center relative to the rotor center in the spanwise and vertical directions is also shown in Fig. 18. For $\theta = 0°$, the spanwise deflection is found to be approximately zero. For positive wind directions, the spanwise deflection is predominantly positive with overall values ranging between $-0.1 < y_0/D < 0.1$. This is consistent with the velocity speedup on one side of the wake, which results in a lateral shift in the wake center towards the opposite side. For $\theta = 15°$ the deflection is the highest, which can be attributed to the strongest velocity speedup on one side of the rotor. For $\theta = -45°$, on the other hand, a significant wake center deflection closer to the turbine can be observed, which reduces with the increase in the streamwise distance but shows a higher magnitude than the majority of the cases. This spanwise wake center deflection in the $\theta = -45°$ is consistent with the merger of the hub vortex with the base flow vortex, as discussed in Sec. III B 1. As the two vortices (hub vortex and base flow vortex) rotate in the same direction, they merge into one in the near wake, resulting in a shift in the wake center. For positive wind directions, these vortices rotate in opposite directions leading to separate vorticity regions in the near wake and relatively less spanwise deflection.

The vertical deflection in the wake center is shown in Fig. 18(d). All cases show a positive deflection of the wake above the rotor center, which is related to the positive vertical velocity experienced by the turbine from the cliff leading edge. For $\theta = 0^\circ$, the vertical deflection is the smallest of all the cases, whereas $\theta = 45^\circ$ shows the highest vertical deflection. For smaller wind directions, $\theta = 0^\circ, 15^\circ$, the vertical deflection is almost constant with the streamwise distance, whereas for $\theta > 15^\circ$, it increases with the increase in the streamwise distance.

4. Streamwise momentum analysis

To further understand the mechanisms behind the recovery of the streamwise momentum in the turbine wake for different wind directions, we examine different terms of the streamwise Reynolds averaged Navier-Stokes (x-RANS) equation. In doing so, we neglect the viscous terms due to high Reynolds number, and no body forces are present in the turbine wake. The RANS equation in the streamwise direction can then be written as [64]

$$U_w \frac{\partial U_w}{\partial x} + V_w \frac{\partial U_w}{\partial y} + W_w \frac{\partial U_w}{\partial z} = -\frac{1}{\rho}\frac{\partial P}{\partial x} - \frac{\partial \overline{u'u'}}{\partial x} - \frac{\partial \overline{u'v'}}{\partial y} - \frac{\partial \overline{u'w'}}{\partial z}, \tag{8}$$

where U_w, V_w, and W_w are the time-averaged streamwise, spanwise, and vertical velocity components in the turbine wake, respectively. Similarly, u', v', and w' are the fluctuating components of the streamwise, spanwise, and vertical velocity, respectively. Analysis of the x-RANS equation has been used in the literature to understand the recovery of streamwise momentum, and flow structures in the wake of yawed or tilted turbines [65,66].

Following Shamsoddin and Porté-Agel [67], Eq. (8) can be written in terms of the streamwise velocity deficit by adding $U_w dU_b/dx$ on both sides. Moreover, the pressure gradient induced by the base flow can be approximated by the streamwise gradient of base flow velocity $U_b dU_b/dx$ [67]. After making the above-mentioned substitutions and rearrangement, the following equation is yielded:

$$\begin{aligned} &\underbrace{U_w \frac{\partial (U_b - U_w)}{\partial x}}_{\text{(I)}} + \underbrace{V_w \frac{\partial (U_b - U_w)}{\partial y}}_{\text{(II)}} + \underbrace{W_w \frac{\partial (U_b - U_w)}{\partial z}}_{\text{(III)}} \\ &= \underbrace{-(U_b - U_w)\frac{dU_b}{dx}}_{\text{(IV)}} + \underbrace{\frac{\partial \overline{u'u'}}{\partial x}}_{\text{(V)}} + \underbrace{\frac{\partial \overline{u'v'}}{\partial y}}_{\text{(VI)}} + \underbrace{\frac{\partial \overline{u'w'}}{\partial z}}_{\text{(VII)}} + \underbrace{W_w \frac{\partial U_b}{\partial z}}_{\text{(VIII)}} + \underbrace{V_w \frac{\partial U_b}{\partial y}}_{\text{(IX)}} + R, \end{aligned} \tag{9}$$

where R is the combination of unaccounted for wake pressure and numerical residuals.

Figure 19 shows the normalized contours of different terms of Eq. (9) at $x/D = 4$ for different wind directions. In general, the terms related to the advection of the streamwise momentum are observed to be affected by the change in the wind direction. Specifically, the induction of a spanwise velocity and development of strong vortices in the wake are responsible for the changes in the advection of the streamwise momentum.

The term $U_w \partial(U_b - U_w)/\partial x$ represents the streamwise advection of the streamwise momentum deficit. This term shows a negative region inside the wake and a positive region on the outer periphery of the wake. As the averaged streamwise velocity is positive, a positive streamwise advection is related to $\partial(U_b - U_w)/\partial x > 0$ indicating a slowdown of the flow due to the cross-stream expansion of the wake with the increase in the streamwise distance. Similarly, a negative streamwise advection can be associated with $\partial(U_b - U_w)/\partial x < 0$, corresponding to the recovery of the streamwise momentum deficit in the wake. Comparing different wind direction cases, the negative region in the core of the wake is strongest for $\theta = \{0^\circ, 15^\circ\}$, the magnitude of which reduces for $\theta > 15^\circ$. This indicates a faster recovery of the streamwise momentum deficit for wind directions $\theta \leqslant 15^\circ$ compared to $\theta > 15^\circ$. This is consistent with the recovery of the wake center streamwise velocity deficit observed in the previous section, where two different recovery rates for $\theta \leqslant 15^\circ$ and $\theta > 15^\circ$

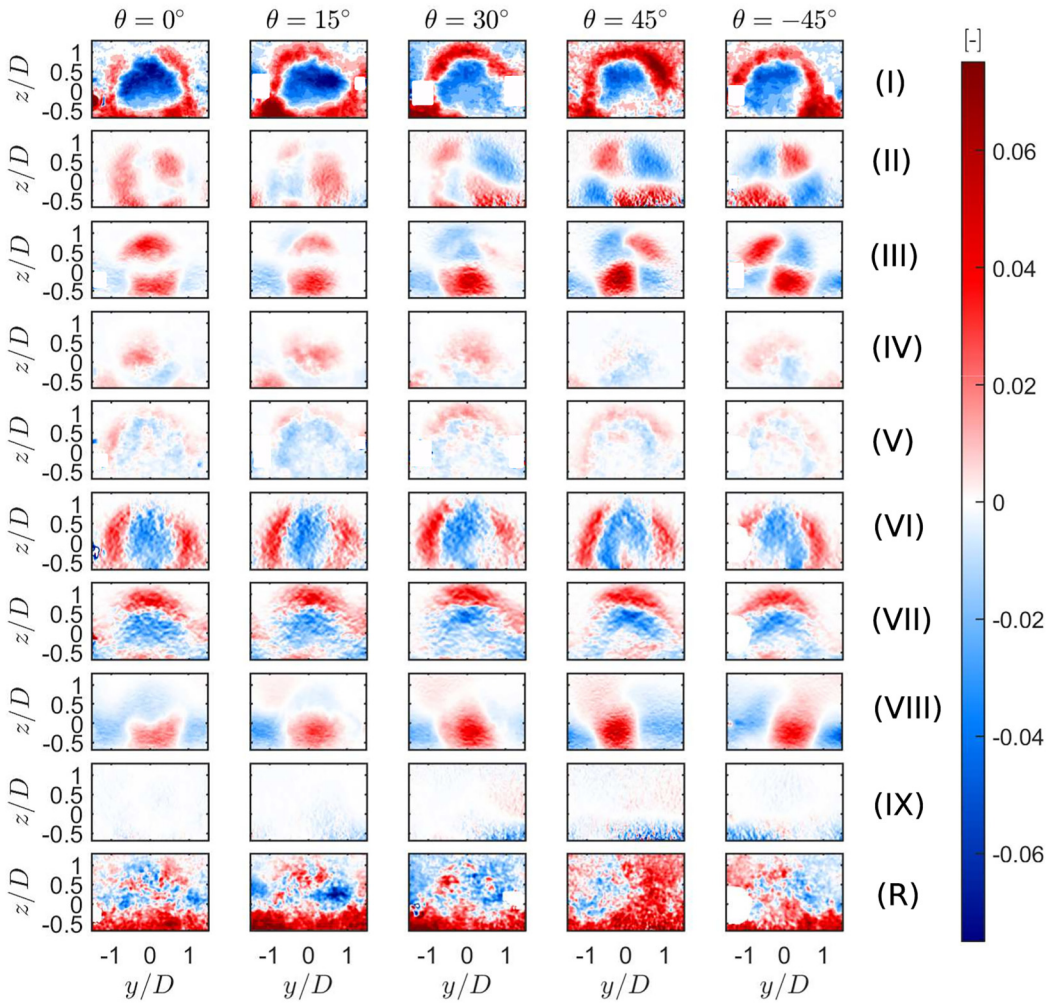

FIG. 19. Contours of the terms of the streamwise momentum equation [Eq. (9)] computed from measurements at $x/D = 4$. All quantities are normalized by D/U_h^2. The white rectangles in some panels crop the noisy data from PIV.

were shown. The spanwise and vertical advection terms ($V_w \frac{\partial(U_b - U_w)}{\partial y}$ and $W_w \frac{\partial(U_b - U_w)}{\partial z}$, respectively) are observed to be significantly affected by the development of streamwise vorticity in the wake. The magnitude of these terms is comparatively smaller than that of the streamwise advection, which is due to the smaller magnitude of the cross-stream velocity components when compared with the streamwise velocity. For $\theta = \{0^\circ, 15^\circ\}$, the cross-stream advection terms are mostly positive, indicating that these terms play a role in bringing higher momentum flow from outside into the wake, thus contributing to its recovery. For wind directions higher than 15°, negative regions start to appear, which could play a role in the slow recovery of the momentum deficit in the wake. For $\theta = \pm 45^\circ$ a quadrupole shape is observed for the cross-stream advection terms, where the spanwise and vertical advection terms show opposite signs. The net effect of the cross-stream advection terms would then depend on the relative magnitude of the individual contributors.

The base flow pressure gradient term is observed to be relatively small, although a positive region in the wake center is observed for most cases. This indicates that the pressure gradient tends to

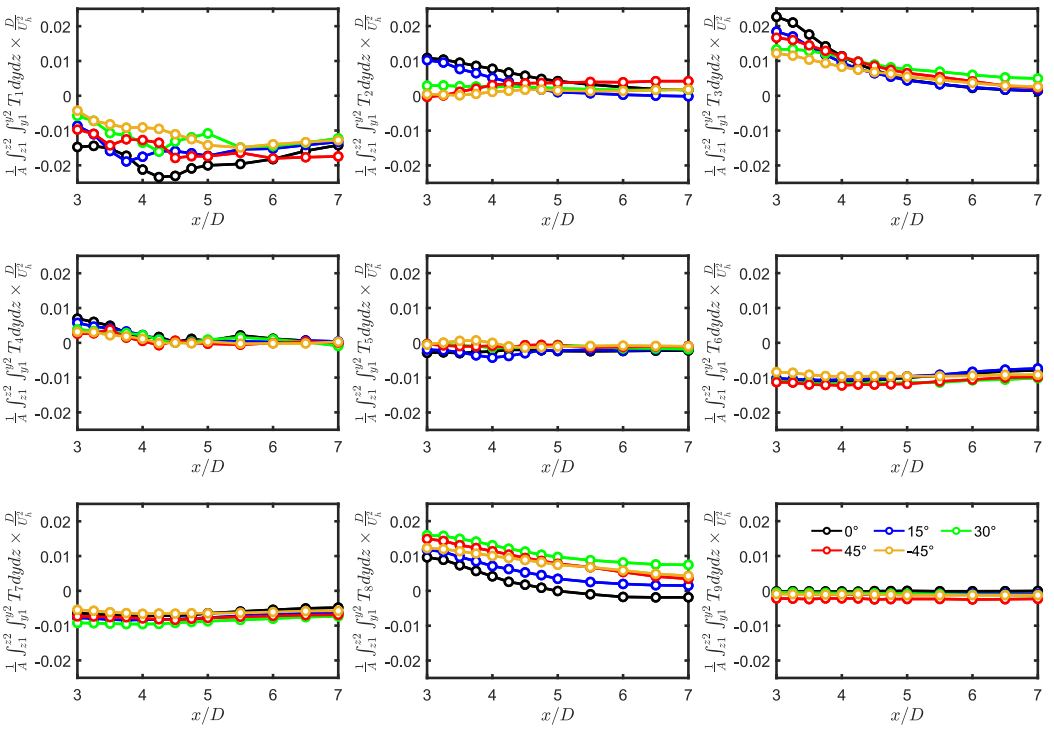

FIG. 20. Term-by-term analysis of the integral of the streamwise momentum terms as a function of streamwise distance.

slow down the recovery of the streamwise momentum deficit. This is understandable, as the cliff induces an adverse pressure gradient on the flow, which is known to slow down the recovery of the turbine wake [4]. The $\partial\overline{u'u'}/\partial x$ term shows the smallest magnitude out of all the terms of the x-RANS equation, and thus, has the smallest contribution to the streamwise momentum in the wake. The observations regarding the pressure gradient term and the streamwise normal Reynolds stress are consistent with previous studies (e.g., [66]). The gradients of the shear stresses, on the other hand, contribute significantly to the momentum recovery in the wake for all wind directions. The gradients of the Reynolds stresses are relatively similar among all cases, both in terms of the spatial distribution and the overall magnitude.

The effect of vertical wind shear (term VIII) is observed to be significant for all wind directions, where the magnitude of the positive region is observed to increase with the wind direction. This is because the cross-stream flow induced by the cliff under different wind directions gets stronger with the increase in the wind direction. Combined with the wake rotation, this helps bring energetic flow from outside into the wake. The effect of lateral heterogeneity in the base flow (term IX) is observed to be relatively very small, indicating that this term does not have a significant contribution to the wake recovery. Finally, the residual term, which includes the unaccounted for wake pressure, shows no trend with the wind direction and has a magnitude comparable to previous studies (e.g., [66]).

Following previous works [68,69], the integral of the streamwise momentum terms is computed according to $\frac{1}{A}\int_{z1}^{z2}\int_{y1}^{y2} T_i dy\, dz$, where $i = 1, 2, ..., 9$ represents each term, and $y1 = z1 = -0.7D$ and $y2 = z2 = 0.7D$. The limit of integration is chosen to capture the characteristic width of the wake. Figure 20 shows the integral for each term. The advection terms are observed to have the highest magnitude out of all the terms. For $\theta \leqslant 15°$, the advection terms show the highest magnitude close to the turbine compared to wind directions greater than 15°. This is consistent with the trend

observed for the wake center recovery, which showed faster recovery for $\theta \leqslant 15^\circ$ cases. The base flow pressure gradient term (T_4) shows high magnitude close to the turbine (and the cliff leading edge) and shows a decrease in the magnitude with the increase in the wind direction close to the turbine. The Reynolds stress terms show similar magnitude for different cases. The vertical wind shear term (T_8), shows an increase in magnitude with the increase in the wind direction, indicating this term's contribution to wake recovery increases with the wind direction. However, the magnitude is comparatively smaller than the advection terms. The lateral gradient of the base flow velocity along with the lateral wake velocity (T_9) shows a near-zero contribution to the wake recovery. This further indicates that change in the advection of the streamwise momentum with the wind direction plays the most significant role in the recovery of the wake.

IV. SUMMARY

Onshore wind energy is currently one of the cheapest available sources of energy. In an onshore environment, terrain complexity plays an important role in determining the performance of a wind farm. Wind turbines are often sited close to cliffs; however, the interaction of flow with the cliff under different wind directions and its influence on a wind turbine wake are not well understood. In this study, we performed comprehensive wind tunnel experiments investigating the flow over a cliff under different incoming wind directions. Moreover, the interaction of this flow with the wake of a wind turbine was also investigated. Five different wind directions were tested: $\theta = \{0^\circ, 15^\circ, 30^\circ, 45^\circ, -45^\circ\}$, where 0° is defined as the wind direction perpendicular to the cliff leading edge.

For flow over the cliff without the turbine, known as the base flow, the flow was observed to become heterogeneous in the spanwise direction with the increase in the wind direction. The streamwise flow recirculation was absent for wind directions above 15°, where a spanwise recirculation was induced with the increase in the wind direction. The normalized turbulence kinetic energy was observed to peak at $\theta = 15^\circ$, which was related to the absence of the streamwise flow recirculation for $\theta > 15^\circ$.

The wake of the wind turbine sited on the cliff was observed to be significantly affected by the change in the wind direction. The development of the spanwise recirculation in the base flow affected the streamwise velocity in the wake: it was symmetric in the spanwise direction for the wind direction perpendicular to the leading edge of the cliff, but became asymmetric with the increase in wind direction. Two important observations made in this regard were the flow speedup on one side of the rotor and the role of the spanwise velocity on the other side of the rotor in pushing the wake in one direction or the other. These features were investigated further by looking at the normalized streamwise vorticity and cross-stream velocity streamlines. The flow speed-up on one side of the rotor was observed to be a result of the formation of a saddle point, which bifurcates the outer base flow from the wake flow and leads to a region of highspeed flow. A counter-rotating vortex pair close to the surface was observed to develop in the far wake for the wind direction perpendicular to the cliff. With the increase in the wind direction, one leg of the CVP grew stronger and dominated the flow, which played a major role in changing the spatial distribution of the streamwise velocity in the wake.

The streamwise wake velocity deficit was quantified using a 2D Gaussian fit. The recovery of the normalized streamwise velocity deficit maximum was observed to slow down for wind directions $\theta > 15^\circ$, which was found to be consistent with the decrease in the base flow turbulence. The wake growth rate was observed to decrease for $\theta > 15^\circ$ compared to $\theta = 0^\circ$, which was consistent with the slower wake recovery in the said cases. The mean wake center in the spanwise and vertical directions was also affected by the wind direction, where the vertical deflection increased with the increase in the positive wind direction. The spanwise wake center position was relatively close to 0 for positive wind directions but showed a high negative deflection for $\theta = -45^\circ$, which was related to the merging of the hub vortex with the base flow vortex in the mentioned case.

A term-by-term analysis of the streamwise x-RANS equation was performed. This analysis revealed differences in the mechanisms of the recovery of the streamwise momentum between different cases. The advection terms in the x-RANS equation showed significant differences between different wind directions. The gradients of Reynolds stresses were largely unaffected by the wind directions. This pointed out that the differences in the recovery of the wake arise from the advection of the streamwise momentum and not from the gradients of the Reynolds stresses.

ACKNOWLEDGMENT

This research was funded by the Swiss National Science Foundation (Grants No. 200021_172538 and No. 200021_215288) and the Swiss Federal Office of Energy (Grant No. SI/502135-01).

[1] IRENA, Renewable power generation costs in 2020, International Renewable Energy Agency, Abu Dhabi (2021).
[2] GWEC, Global wind report 2021, Global Wind Energy Council (2021).
[3] R. Stevens and C. Meneveau, Flow structure and turbulence in wind farms, Annu. Rev. Fluid Mech. **49**, 311 (2017).
[4] F. Porté-Agel, M. Bastankhah, and S. Shamsoddin, Wind-turbine and wind-farm flows: A review, Boundary Layer Meteorol. **174**, 1 (2020).
[5] P. Alfredsson and A. Segalini, Introduction wind farms in complex terrains: An introduction, Philos. Trans. R. Soc. A **375**, 20160096 (2017).
[6] G. Taylor and D. Smith, Wake measurements over complex terrain, in *Proceedings of the 13th BWEA Conference: Wind Energy Conversion* (Mechanical Engineering Publications, London, 1991), pp. 10–12.
[7] N. Stefanatos, S. Voutsinas, K. Rados, A. Zervos, and J. Tsipouridis, A combined experimental and numerical investigation of wake effects in complex terrain, in *Proceedings of EWEC* (GWEC, Thessaloniki, Greece, 1994), Vol. 94, pp. 484–490.
[8] C. Helmis, K. Papadopoulos, D. Asimakopoulos, P. Papageorgas, and A. Soilemes, An experimental study of the near-wake structure of a wind turbine operating over complex terrain, Solar Energy **54**, 413 (1995).
[9] P. Jackson and J. Hunt, Turbulent wind flow over a low hill, Q. J. R. Meteorol. Soc. **101**, 929 (1975).
[10] P. Mason and R. Sykes, Flow over an isolated hill of moderate slope, Q. J. R. Meteorol. Soc. **105**, 383 (1979).
[11] R. Sykes, An asymptotic theory of incompressible turbulent boundary layer flow over a small hump, J. Fluid Mech. **101**, 647 (1980).
[12] R. Britter, J. Hunt, and K. Richards, Air flow over a two-dimensional hill: Studies of velocity speed-up, roughness effects and turbulence, Q. J. R. Meteorol. Soc. **107**, 91 (1981).
[13] P. Taylor, P. Mason, and E. Bradley, Boundary-layer flow over low hills, Boundary Layer Meteorol. **39**, 107 (1987).
[14] D. Xu, K. Ayotte, and P. Taylor, Development of a non-linear mixed spectral finite difference model for turbulent boundary-layer flow over topography, Boundary Layer Meteorol. **70**, 341 (1994).
[15] P. Taylor and H. Teunissen, The Askervein Hill project: Overview and background data, Boundary Layer Meteorol. **39**, 15 (1987).
[16] J. Berg, J. Mann, A. Bechmann, M. Courtney, and H. Jørgensen, The Bolund experiment, Part I: Flow over a steep, three-dimensional hill, Boundary Layer Meteorol. **141**, 219 (2011).
[17] P. Mason, Large-eddy simulation: A critical review of the technique, Q. J. R. Meteorol. Soc. **120**, 1 (1994).
[18] W. Gong, P. Taylor, and A. Dörnbrack, Turbulent boundary-layer flow over fixed aerodynamically rough two-dimensional sinusoidal waves, J. Fluid Mech. **312**, 1 (1996).
[19] A. Bechmann, N. Sørensen, J. Berg, J. Mann, and P.-E. Réthoré, The Bolund experiment, Part II: Blind comparison of microscale flow models, Boundary Layer Meteorol. **141**, 245 (2011).
[20] F. Wan and F. Porté-Agel, Large-eddy simulation of stably-stratified flow over a steep hill, Boundary Layer Meteorol. **138**, 367 (2011).

[21] M. Diebold, C. Higgins, J. Fang, A. Bechmann, and M. Parlange, Flow over hills: A large-eddy simulation of the bolund case, Boundary Layer Meteorol. **148**, 177 (2013).
[22] L. Liu and R. Stevens, Wall modeled immersed boundary method for high Reynolds number flow over complex terrain, Comput. Fluids **208**, 104604 (2020).
[23] J. Finnigan, K. Ayotte, I. Harman, G. Katul, H. Oldroyd, E. Patton, D. Poggi, A. Ross, and P. Taylor, Boundary-layer flow over complex topography, Boundary Layer Meteorol. **177**, 247 (2020).
[24] J. Mattuella, A. Loredo-Souza, M. Oliveira, and A. Petry, Wind tunnel experimental analysis of a complex terrain micrositing, Renewable Sustainable Energy Rev. **54**, 110 (2016).
[25] W. Tian, A. Ozbay, W. Yuan, P. Sarakar, H. Hu, and W. Yuan, An experimental study on the performances of wind turbines over complex terrain, in *51st AIAA Aerospace Sciences Meeting Including the New Horizons Forum and Aerospace Exposition, Texas, USA* (American Institute of Aeronautics and Astronautics, Reston, VA, 2013), pp. 7–10.
[26] X. Yang, K. Howard, M. Guala, and F. Sotiropoulos, Effects of a three-dimensional hill on the wake characteristics of a model wind turbine, Phys. Fluids **27**, 025103 (2015).
[27] A. Hyvärinen and A. Segalini, Qualitative analysis of wind-turbine wakes over hilly terrain, J. Phys.: Conf. Ser. **854**, 012023 (2017).
[28] S. Shamsoddin and F. Porté-Agel, Wind turbine wakes over hills, J. Fluid Mech. **855**, 671 (2018).
[29] R. Menke, K. Vasiljević, N. Hansen, A. Hahmann, and J. Mann, Does the wind turbine wake follow the topography? A multi-lidar study in complex terrain, Wind Energy Sci. **3**, 681 (2018).
[30] A. S. Dar, J. Berg, N. Troldborg, and E. Patton, On the self-similarity of wind turbine wakes in a complex terrain using large eddy simulation, Wind Energy Sci. **4**, 633 (2019).
[31] L. Liu and R. Stevens, Effects of two-dimensional steep hills on the performance of wind turbines and wind farms, Boundary Layer Meteorol. **176**, 251 (2020).
[32] Z. Liu, S. Lu, and T. Ishihara, Large eddy simulations of wind turbine wakes in typical complex topographies, Wind Energy **24**, 857 (2021).
[33] A. S. Dar, A. S. Gertler, and F. Porté-Agel, An experimental and analytical study of wind turbine wakes under pressure gradient, Phys. Fluids **35**, 045140 (2023).
[34] X. Han, D. Liu, C. Xu, and W. Shen, Atmospheric stability and topography effects on wind turbine performance and wake properties in complex terrain, Renewable Energy **126**, 640 (2018).
[35] L. Liu and R. Stevens, Effects of atmospheric stability on the performance of a wind turbine located behind a three-dimensional hill, Renewable Energy **175**, 926 (2021).
[36] W. Radünz, Y. Sakagami, R. Haas, A. Petry, J. Passos, M. Miqueletti, and E. Dias, Influence of atmospheric stability on wind farm performance in complex terrain, Appl. Energy **282**, 116149 (2021).
[37] F. I. Pacheco de Sá Sarmiento, J. Oliveira, and J. Passos, Impact of atmospheric stability, wake effect and topography on power production at complex-terrain wind farm, Energy **239**, 122211 (2022).
[38] J. Rowcroft, D. Burton, H. Blackburn, and J. Sheridan, Siting wind turbines near cliffs: The effect of ruggedness, J. Fluids Eng. **141**, 031104 (2019).
[39] A. Bowen and D. Lindley, A wind-tunnel investigation of the wind speed and turbulence characteristics close to the ground over various escarpment shapes, Boundary Layer Meteorol. **12**, 259 (1977).
[40] J. Lange, J. Mann, J. Berg, D. Parvu, R. Kilpatrick, A. Costache, J. Chowdhury, K. Siddiqui, and H. Hangan, For wind turbines in complex terrain, the devil is in the detail, Environ. Res. Lett. **12**, 094020 (2017).
[41] C. Schulz, L. Klein, P. Weihing, and T. Lutz, Investigations into the interaction of a wind turbine with atmospheric turbulence in complex terrain, J. Phys.: Conf. Ser. **753**, 032016 (2016).
[42] G.-W. Qian and T. Ishihara, Numerical study of wind turbine wakes over escarpments by a modified delayed detached eddy simulation, J. Wind Eng. Ind. Aerodyn. **191**, 41 (2019).
[43] A. S. Dar and F. Porté-Agel, Three-dimensional wind-turbine wake characterization via tomographic particle-image velocimetry, J. Phys.: Conf. Ser. **1618**, 062045 (2020).
[44] A. S. Dar and F. Porté-Agel, Wind turbine wakes on escarpments: A wind-tunnel study, Renewable Energy **181**, 1258 (2022).

[45] A. S. Dar and F. Porté-Agel, An analytical model for wind turbine wakes under pressure gradient, Energies **15**, 5345 (2022).
[46] J. Largeau and V. Moriniere, Wall pressure fluctuations and topology in separated flows over a forward-facing step, Exp. Fluids **42**, 21 (2007).
[47] M. Sherry, D. Jacono, and J. Sheridan, An experimental investigation of the recirculation zone formed downstream of a forward facing step, J. Wind Eng. Ind. Aerodyn. **98**, 888 (2010).
[48] H. Ren and Y. Wu, Turbulent boundary layers over smooth and rough forward-facing steps, Phys. Fluids **23**, 045102 (2011).
[49] M. Awasthi, W. Devenport, S. Glegg, and J. Forest, Pressure fluctuations produced by forward steps immersed in a turbulent boundary layer, J. Fluid Mech. **756**, 384 (2014).
[50] A. Graziani, M. Lippert, D. Uystepruyst, and L. Keirsbulck, Scaling and flow dependencies over forward-facing steps, Int. J. Heat Fluid Flow **67**, 220 (2017).
[51] A. Graziani, F. Kerhervé, R. Martinuzzi, and L. Keirsbulck, Dynamics of the recirculating areas of a forward-facing step, Exp. Fluids **59**, 154 (2018).
[52] J. Rowcroft, D. Burton, H. Blackburn, and J. Sheridan, Siting wind turbines near cliffs—The effect of wind direction, Wind Energy **19**, 1469 (2016).
[53] R. Barthelmie and S. Pryor, The impact of wind direction yaw angle on cliff flows, Wind Energy **21**, 1254 (2018).
[54] P. Hesp and T. Smyth, CFD flow dynamics over model scarps and slopes, Phys. Geogr. **42**, 1 (2021).
[55] M. Bastankhah and F. Porté-Agel, A new miniature wind turbine for wind tunnel experiments. Part I: Design and performance, Energies **10**, 908 (2017).
[56] G. Bergeles and N. Athanassiadis, The flow past a surface-mounted obstacle, J. Fluids Eng. **105**, 461 (1983).
[57] H. Zong and F. Porté-Agel, A point vortex transportation model for yawed wind turbine wakes, J. Fluid Mech. **890**, A8 (2020).
[58] B. Wieneke, PIV uncertainty quantification from correlation statistics, Meas. Sci. Technol. **26**, 074002 (2015).
[59] Y.-M. Saint-Drenan, R. Besseau, M. Jansen, I. Staffell, A. Troccoli, L. Dubus, J. Schmidt, K. Gruber, S. G. Simões, and S. Heier, A parametric model for wind turbine power curves incorporating environmental conditions, Renewable Energy **157**, 754 (2020).
[60] E. Essel and M. Tachie, Upstream roughness and Reynolds number effects on turbulent flow structure over forward facing step, Int. J. Heat Fluid Flow **66**, 226 (2017).
[61] Y.-T. Wu and F. Porté-Agel, Atmospheric turbulence effects on wind-turbine wakes: An LESstudy, Energies **5**, 5340 (2012).
[62] M. Bastankhah and F. Porté-Agel, A new miniature wind turbine for wind tunnel experiments. Part II: Wake structure and flow dynamics, Energies **10**, 923 (2017).
[63] P. Brugger, F. Fuertes, M. Vahidzadeh, C. Markfort, and F. Porté-Agel, Characterization of wind turbine wakes with nacelle-mounted Doppler LiDARs and model validation in the presence of wind veer, Remote Sens. **11**, 2247 (2019).
[64] S. Pope, *Turbulent Flows* (Cambridge University Press, Cambridge, UK, 2000).
[65] M. Bastankhah and F. Porté-Agel, Experimental and theoretical study of wind turbine wakes in yawed conditions, J. Fluid Mech. **806**, 506 (2016).
[66] J. Bossuyt, R. Scott, N. Ali, and R. Cal, Quantification of wake shape modulation and deflection for tilt and yaw misaligned wind turbines, J. Fluid Mech. **917**, A3 (2021).
[67] S. Shamsoddin and F. Porté-Agel, A model for the effect of pressure gradient on turbulent axisymmetric wakes, J. Fluid Mech. **837**, R3 (2018).
[68] G. Dong, J. Qin, Z. Li, and X. Yang, Characteristics of wind turbine wakes for different blade designs, J. Fluid Mech. **965**, A15 (2023).
[69] D. Siguenza-Alvarado, V. Pulletikurthi, J. J. Quinones, C. Nelson, S. Cheng, A. Doosttalab, L. P. Chamorro, and L. Castillo, Wake interaction of aligned wind turbines over two-dimensional hills, Phys. Fluids **35**, 105142 (2023).